Experiments in Fluids (2024) 65:144
https://doi.org/10.1007/s00348-024-03876-z

REVIEW

Characterization of a hypersonic turbulent boundary layer along a sharp cone with smooth and transverse square−bar roughened wall

Dominik Neeb[1] · **Pascal Marquardt**[2] · **Ali Gülhan**[3]

Received: 22 February 2024 / Revised: 26 June 2024 / Accepted: 21 August 2024

Abstract

In the present study, the response of a hypersonic turbulent boundary layer at an inflow of $Ma_\infty = 6$ and $Re_\infty = 16{\cdot}10^6$ 1/m to a smooth and rough surface along a sharp cone is examined. The model consisted of three segments with exchangeable parts to consider smooth and rough surfaces with a roughness topology of square bar elements with a nominal wavelength of four times the height of the elements. In selected regions of interest, the flow field was measured by particle image velocimetry (PIV) which enabled analysis of mean velocity fields and Reynolds stresses. Van Driest transformed smooth wall mean velocity profiles showed the expected incompressible behavior and compared well to previous investigations. A combination of an integral and fitting approach is discussed to enable inner scaling of the rough wall profiles, which showed the expected shift below the smooth wall profile. The smooth wall turbulence profiles from PIV agreed to artificially filtered DNS in case of the streamwise component. Turbulence profiles above the smooth and rough wall agreed to within measurement accuracies. Additionally, two−point correlations were used to investigate turbulent structures above the smooth and rough wall. Both, length scales and orientations of the correlations, showed high level of agreement between smooth and rough walls, with only differences close to the wall. Furthermore, uniform momentum zones could be identified with similar behavior along both smooth and rough walls. Information from turbulence data support outer layer similarity, whereas mean velocity profiles show an increase in Coles wake parameter for the rough wall data. This might be influenced by transitional roughness effects.

1 Introduction

Surface roughness has an impact on different aspects of the boundary layer which evolves along high−speed flight vehicles, e.g., the laminar−to−turbulent transition process. For an already turbulent boundary layer (TBL) roughness can increase skin friction drag and convective heat transfer above the turbulent levels. These roughness augmentation effects need to be considered for the design of such vehicles and the quantification and understanding of the roughness impact on turbulent boundary layers is of high importance to leverage prediction capabilities.

Fundamental work investigating roughness induced augmentation effects in incompressible flow have been performed by Nikuradse (1933) and Schlichting (1936). Schlichting introduced an equivalent sand grain roughness parameter to link his results on a variety of technical roughness patterns to the scaling laws found by Nikuradse. The defining parameter is the roughness Reynolds number $k_s^+ = k_s u_\tau / \nu_w$ where k_s is the equivalent sand grain roughness (EQSR), the skin friction velocity $u_\tau = \sqrt{\tau_w / \rho_w}$, in which τ_w is the shear stress at the wall and ν_w and ρ_w are the kinematic viscosity and density at the wall, respectively. Depending on the EQSR Reynolds number k_s^+, three different regimes can be differentiated with a hydraulically smooth, a transitional and a fully rough regime, the latter of which typically defined with $k_s^+ \geq 60 - 70$.

Among the first to perform detailed compressible investigations were Goddard (1957) and Berg (1977). The work

✉ Dominik Neeb
dominik.neeb@dlr.de

[1] Research Scientist at Supersonic and Hypersonic Flow Technologies Department, German Aerospace Center (DLR), Institute of Aerodynamics and Flow Technology, Cologne, Germany

[2] Research Scientist at Hypersonic Flow Technologies Department, German Aerospace Center (DLR), Institute of Aerodynamics and Flow Technology, Cologne, Germany

[3] Head of Hypersonic Flow Technologies Department, German Aerospace Center (DLR), Institute of Aerodynamics and Flow Technology, Cologne, Germany

Published online: 18 September 2024

of the latter is one of a few investigations which studied the mean and turbulent flow characteristics of a compressible TBL along transverse square bar rough walls of similar shape to the one of interest in this paper. This kind of technical roughness exhibits a topology with consecutive bars with square cross sections in the streamwise direction (width equals height, see also Fig. 2) spanning the full model dimension in the direction transverse to the main flow. This shape was widely investigated since it is well defined, typically easy to manufacture and shows high roughness impact on the flow (depending on the choice of certain dimensions). Berg (1977) studied the TBL at $Ma_e \approx 6$ and $Re_\theta = U_e\theta/\nu_e = 63000$, with the edge velocity U_e, the momentum loss thickness θ and the kinematic viscosity at the boundary layer edge ν_e. He tested along smooth and rough walls with transverse square bars of $\lambda/k = 4$, with the physical roughness height k and the wavelength of the roughness topology λ. This resulted in $k^+ = 7.1, 14, 33.8$ and $k/\delta = 0.012, 0.025, 0.04$, respectively, with the boundary layer thickness δ (here defined where the velocity reaches 99% of the edge velocity). Additionally to mean velocity profiles from Pitot pressure measurements, he also investigated fluctuating properties via hot−wire measurements. He was able to successfully scale his mean velocity profiles via the van Driest transformation and extracted with $k_s/k = 1.3$ one of the lowest EQSR for this type of roughness in contrast to incompressible values (e.g., Perry and Joubert 1963 $k_s/k = 2.3$–2.5, Bettermann 1966 $k_s/k = 2.7$, Liu et al. 1966 $k_s/k = 2.0$–2.6, Krogstadt and Antonia 1999 $k_s/k = 6.0$). Since he also studied the transition from smooth to a rough surface, Berg found a new equilibrium profile for both mean and fluctuating profiles after approximately $10-25\ \delta$ downstream of the step change from smooth to rough.

Sahoo et al. performed PIV measurements on TBL along smooth and rough flat plate models at $Ma_e \approx 7.3$ and $Re_\theta \approx 3900$ and 5500 with square bar roughness of $\lambda/k = 5$ (Sahoo et al. 2010, 2009). In both publications, values are reported with $k^+ = 102, 134$, $k/\delta = 0.14, 0.12$ and $k_s/k = 5.9, 4.5$, respectively. Besides the success of van Driest mean velocity scaling and the expected downward shift due to roughness, the streamwise and wall−normal inner−scaled fluctuations were reported to be damped in presence of the rough wall.

Latin and Bowersox (2000) and Pritchett and Bowersox (2001) studied transverse square bar roughness of $\lambda/k = 3.9$ at $Ma_e = 2.7$ and $Ma_e = 0.56, 0.22$, respectively. Values of $k^+ = 148.5, 867, 837$ and $k_s/k = 1.9, 0.6, 0.6$ were reported for the three different Mach numbers, respectively. In mean and turbulent flow profiles, local distortions caused by the square bar roughness were much less significant compared to also investigated mesh roughness topology, which produced a pattern of oblique shocks and expansion waves, which could penetrate through much of the boundary layer and therefore questioning comparisons to incompressible counterparts.

Williams et al. performed PIV measurements on a TBL at $Ma_e \approx 7.2 - 7.6$ and $Re_\tau = 180 - 679$ along smooth and rough flat plate models (Williams et al. 2018, 2021). This included the investigation of transverse square bar roughness with $\lambda/k = 8.33, 10.63, 5$ which resulted in $k^+ = 30, 70, 112$, $k/\delta = 0.068, 0.098, 0.165$ and $k_s/k = 0.7, 2.3, 3.3$, respectively. Along the smooth wall, the mean and fluctuating streamwise velocity profiles showed strong similarity in the outer layer to incompressible flows at comparable Reynolds numbers when scaled according to van Driest and Morkovin. In case of the rough wall data (Williams et al. 2021), mean van Driest transformed velocity profiles supported the outer layer similarity hypothesis after Townsend (1976), which states that the outer flow is unaffected except in the role the roughness plays in determining the outer velocity and length scales (Jiménez 2004). This was confirmed although the Reynolds numbers were comparably moderate and the roughness large in terms of k/δ compared to a value of 0.025, which is thought to be the limit for a roughness effect being confined to within the inner parts of the TBL according to Jiménez (2004). There is on−going debate about the applicability and limits for outer layer similarity even for incompressible flows (e.g., Castro et al. 2013; Flack et al. 2007; Antonia and Djenidi 2010; Schultz and Flack 2005). Williams et al. showed two−point correlations of PIV velocity fields to reveal that streamwise correlation lengths and structure angles were less sensitive to compressibility than indicated before by mass−flux hot−wire measurements, which are influenced by density. This result indicated different driving length scales for velocity and density fields at high Mach numbers. The outer layer length scales as well as structure angles agreed between smooth and rough wall data within the corresponding data scatter. Also, instantaneous PIV velocity fields along the smooth wall revealed uniform momentum zones (UMZ), which have been observed in different incompressible investigations and have been attributed to the general concept of hairpin vortex structures (Adrian et al. 2000). Williams et al. identified a mean number of UMZs similar to incompressible boundary layers at comparable Reynolds numbers.

Here, we report measurements along a 7° sharp cone with and without two−dimensional transverse square bar roughness with $\lambda/k \approx 4$, $k/\delta \approx 0.1$ and $k^+ \approx 30 - 40$, sometimes labeled as 'large' or 'strong roughness.' PIV was used to measure the mean velocities and turbulent quantities but also to investigate the structure of the TBL. The main objective was to investigate the impact of large roughness in a high Mach number TBL and the possibility if outer layer similarity might still hold. Additionally, an effort was made to extract the equivalent sand grain roughness from the mean

velocity profiles and assess inner−scaling fitting routines for rough wall profiles.

If not otherwise stated, the axial, wall−parallel and wall−normal directions are denoted in the following by x_a, x and y, respectively. Velocities denoted by U correspond to the x and V to the y−direction. Furthermore, mean velocities are denoted by a capital letter (U, V), while instantaneous velocities are the corresponding lowercase letters (u, v). The fluctuating velocities are denoted by an additional bar (u', v') and an overbar indicates ensemble averaging (e.g., $\overline{u'u'}$). Superscript + indicates normalization using viscous length and velocity scales which are ν_w/u_τ and u_τ, respectively.

2 Methods

In the following all methods which supported the analysis in this paper are summarized. First the analytical and numerical tools, then the experimental tools and finally the post−processing methods are presented.

2.1 Analytical and numerical tools

The nominal edge conditions were derived by the Taylor–Maccoll equation (see, e.g., Anderson 1990), assuming negligible influence of a thin boundary layer.

CFD calculations were performed with the DLR TAU code. The TAU code is a finite volume Euler/Navier–Stokes solver, which can use structured, unstructured and hybrid meshes, and has already been applied and validated on studies of various configurations in various flow regimes, including hypersonic flow (Hannemann 2002). In case of turbulent computations, a one−equation Spalart–Allmaras model with Edwards modification (SAE), a two−equation Wilcox−k−ω−model and a seven−equation Reynolds stress model (RSM) with a hybrid Speziale−Sarkar−Gatski/Launder−Reece−Rodi (SSG/LRR−ω) model was used. If not otherwise noted, a turbulent Prandtl number of $Pr_t = 0.9$ was assumed in all applied models. This choice is supported by DNS data according to Duan et al. (2010). A dedicated grid convergence analysis was performed and reported in Neeb et al. (2018).

2.2 Experimental tools

2.2.1 Wind tunnel

Experiments have been performed in the DLR hypersonic wind tunnel (H2K) in Cologne. The facility is an intermittently working blow down tunnel with a free jet test section. Depending on the flow condition, test durations up to 30s can be achieved. The facility is equipped with five exchangeable contoured nozzles with an exit diameter of 600 mm, i.e., $Ma = 5.3$; 6.0; 7.0; 8.7; 11.2. To avoid air condensation as well as to operate the facility at high stagnation temperatures, electrical heaters with a capacity of up to 5 MW are integrated upstream of the nozzle. Unit Reynolds numbers between $2.5{\cdot}10^6$ and $20{\cdot}10^6$ m^{-1} can be set by varying the stagnation pressure p_0 and stagnation temperature T_0. The range of achievable Reynolds numbers at the five discrete Mach numbers can be seen in the performance map in Fig. 1. The uncertainties of the inflow conditions are based on calibrations of the corresponding instrumentation and can be given with $U_{p0} = \pm 0.1\%$ (full scale of $p_0 = 70$ bar), $U_{T0} = \pm 1.1$ °C or $\pm 0.4\%$ (whichever is higher) and $U_{Ma} = \pm 0.04$.

2.2.2 Model

A sharp right−circular cone model was chosen with a half opening angle of 7°. The model consisted of three exchangeable segments. The first segment consisted of a sharp metallic nose with a radius in the order of 0.1 mm. All other segments were made of Polyether ether ketone (PEEK), which is a colorless organic high temperature polymer thermoplastic. It is the standard material for surface temperature measurements via infrared thermography in H2K, due to detailed knowledge of the temperature dependent material properties. To separate effects of roughness induced transition and roughness induced turbulent augmentation effects, a turbulent boundary layer approaching the roughness elements needed to be realized. In previous test campaigns on smooth 7° sharp cones, the transition front established at a Reynolds number which is reached at the middle segment of the current cone model (Willems, et al. 2014). Therefore, it was decided to apply the surface roughness only along the aft segment. A technical roughness pattern was applied, based on previous measurements within the ExoMars

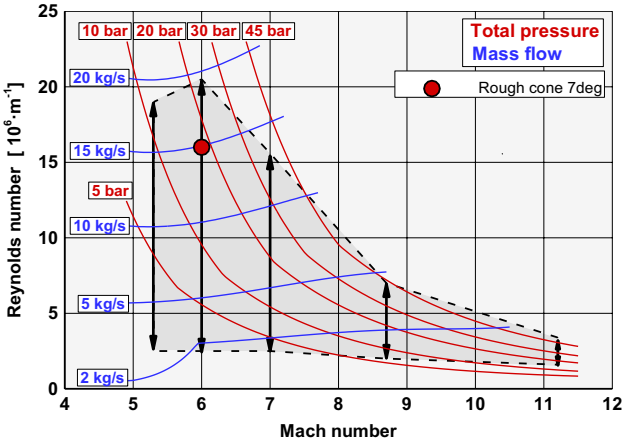

Fig. 1 Hypersonic wind tunnel H2K performance map, including test condition

campaign (Neeb et al. 2016). It consisted of a square bar pattern with a wavelength λ to width w or height k ratio of nominally $\lambda/w=(w+i)/w=(w+i)/k=4$, with the bar interval i. The nominal bar height k and width w was 0.5 mm (see Fig. 2). The top of each square bar was aligned with the smooth part of the model. A smooth wall end segment was used to extract reference data. The total length of the model was $L=0.73$ m with an end diameter of $D=0.18$ m. The roughness pattern begins at $x_a=0.326$ m ($x_a/L=0.44$) and ends at $x_a=0.65$ m ($x_a/L=0.89$), so that approximately the last 80 mm of the rough wall segment has also a smooth wall (originally designed to include local sensors).

The model surface roughness and outer mold line were checked after manufacturing via an optical chromatic distance measurement device with an accuracy typically below 2 µm. The roughness of the smooth PEEK parts had an inner scaled roughness of $R^+_{max} \approx 1.1$, which is well below a value of 5, typically stated as upper limit of a hydraulically smooth surface (Schlichting 1936). Several different 20×20 mm^2 sectors along the rough segment were optically measured and statistically evaluated. Additionally, calibrated PIV images can be exploited to extract the contour in the PIV field of views (FOV). Scans and PIV data suggest that the roughness changes slightly along the axial direction. Along the upstream part, values of typically $k = 0.46 \pm 0.03$ mm, $b = 0.51 \pm 0.02$ m m , $i = 1.49 \pm 0.02$ m m , $\lambda = 2.00 \pm 0.02$ mm and $\lambda/k = 4.34 \pm 0.34$ were measured from scans. Along the downstream part slightly lower values for k were measured. This tendency was also visible

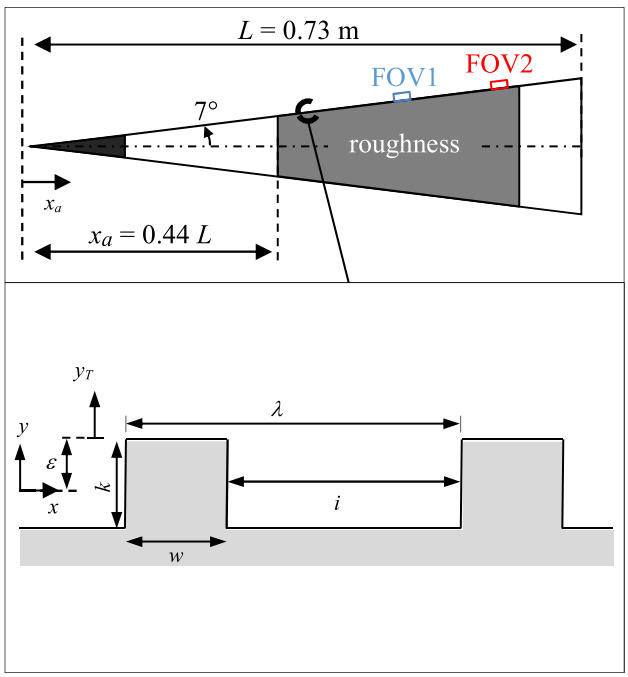

Fig. 2 Definition of model and technical roughness pattern

in the PIV images with $k = 0.5 \pm 0.01$ mm at FOV1 and $k = 0.43 \pm 0.01$ mm at FOV2 (see also Fig. 2). Although it needs to be mentioned that the reported uncertainties for k are of the same magnitude as the resolution uncertainty of the PIV setup, so that corresponding values might be larger.

The model was fixated by a typical sting configuration and placed in a short distance downstream of the wind tunnel nozzle exit. This enabled a set−up with one IR camera view from top of the test chamber, one IR camera view from atop of the nozzle within the test chamber and an optical set−up within the test chamber for PIV. For both IR cameras a suitable window was applied, transparent within the IR regime. The data of the IR cameras were used to calculate convective heat flux along the cone model (not reported in this paper). At the same time, IR data was used to measure wall temperatures with an accuracy of ± 5 K which was used during post−processing to derive e.g. wall densities or skin friction velocities.

2.2.3 Surface pressure

The wind tunnel model was equipped with pressure holes with a diameter of 0.5 mm at nine different positions. Pressure taps were located at three different axial sections along the model, at $x_a=0.25$, 0.495 and 0.651 m. In the first and last section, four different taps were positioned with an angular distance of 90°. This setup enabled the analysis of model alignment and pressure gradients along the surface. The taps were connected via steel and flexible tubing to a miniature electronic pressure scanner (ESP) outside the wind tunnel model with a measurement range of 34.5 kPa (5 psi). In case of the mid−axial location of the rough wall section, small smooth wall plateaus (rectangular cross section with 8×16 mm^2) were foreseen. In this work the pressure was assumed constant throughout the TBL and therefore, the surface pressure was also used in post−processing of the data (e.g., as edge pressure which also influences the density and therefore edge−based Reynolds numbers as well as skin friction velocities via the wall densities).

2.2.4 Particle image velocimetry (PIV)

Streamwise and wall−normal velocities were obtained using two−dimensional, two−component PIV. A SpitLight DPSS 250 PIV Laser system of InnoLas Laser GmbH was used as light source. It is a diode−pumped solid−state laser (Nd:YAG) at 532 nm and has a pulse rate of 100 Hz and a maximum energy of 120 mJ per pulse. The laser was operated at maximum power with an additional attenuator to control the incident power in the test section. The laser pulse timing was monitored during tests with a photo diode measurement and the uncertainty was estimated to approximately ± 1.5 ns. Through a flange, equipped with a suitable

window for the corresponding laser wavelength, the beam was directed toward the wind tunnel model via an optical set−up. It was fixed to the top of the wind tunnel test section and consisted of three lenses, one of which was a cylindrical one. The final laser sheet along the model surface had a nominal length (in axial direction) of larger than 20 mm and a thickness (in lateral direction) of approximately 1 mm. The set−up inside the test section is visible in Fig. 3a.

For the acquisition of images, two LaVison Imager sCMOS cameras with a pixel (pix) size of 6.5 µm were used. A long−distance microscope K2 Distamax from Infinity Photo−Optical was used on both cameras via a beam splitter. With a CF−1b lens, a magnification of approximately 113 pix/mm was accomplished. The images were de−warped based on the calibration with a final magnification of 128 pix/mm. The images were recorded at a size of 2560×1060 pix^2 to enable acquisition rates of 50 Hz for each camera. With proper timing, i.e., both cameras recorded images in an alternating order, the laser system could be used at 100 Hz repetition rate since both cameras shared

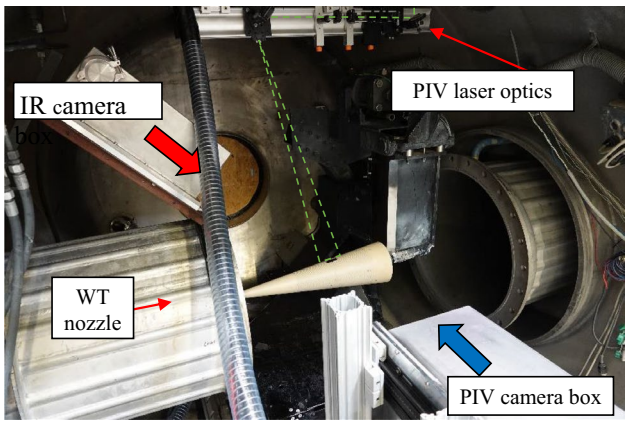

a)

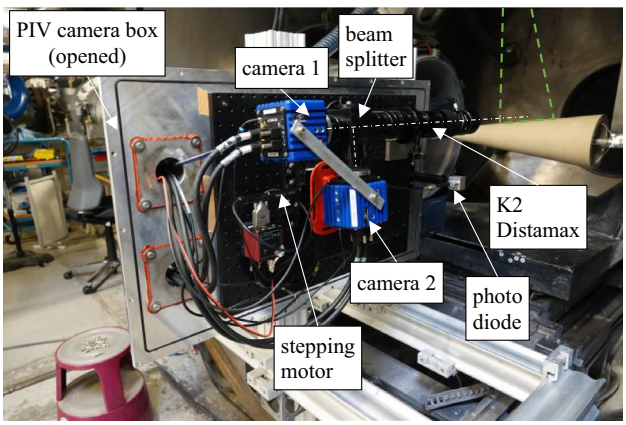

b)

Fig. 3 Set−up in H2K test section with **a** closed and **b** opened sealed PIV camera box

the FOV via the beam splitter. The complete camera setup was installed in a sealed box within the H2K test section to be as close to the target and yet isolated from the vacuum condition in the test section (see Fig. 3b). With this setup a FOV of approximately 20 mm in streamwise and 8 mm in wall−normal direction (approximately 5 $\delta \times 2\ \delta$) was recorded. From these two 2D fields, averaged 1D profiles were extracted approximately at the mid position of the FOV at $x_d/L = 0.68$ and $x_d/L = 0.85$, called in the following measurement section MS1 and MS2, respectively (see Fig. 2). MS1 is located 170 mm behind the beginning of the rough segment which resulted in approximately 48 times the smooth wall boundary layer height at MS1. This is well above the value of 10–25 stated by Berg to be necessary to reach a new boundary layer equilibrium condition downstream a smooth to rough wall topology change (Berg 1977).

For seeding, a Solid Particle Generator was used, which was connected to the settling chamber of the H2K wind tunnel. With this approach, a homogeneous seeding in the test section could be realized. TiO_2 particles of type 1002 from the company KRONOS INTERNATIONAL INC. were used. The manufacturer states a median diameter of $d_p \approx 0.2$—0.3 µm and a density of $\rho_p \approx 3800$ kg/m^3. Before seeding, the particles were sieved and dried in an oven to counteract agglomeration. Previous investigations at the same inflow conditions, which also considered potential agglomerations, resulted in Stokes numbers $S_k = \tau_p/(10\delta/U_e)$ in a range of $0.4 < S_k < 1.5$ with an expected reduction in streamwise rms turbulence intensity of approximately 8–15% (Neeb et al. 2018). This estimation was based on a computational approach, which simulates the particle response to velocity fluctuations based on different drag formulations according to Williams et al. (2015). Comparable Stokes numbers were estimated before and although clear particle lag effects were seen for the wall−normal component, only limited effects were visible for the streamwise component (Williams et al. 2018; Neeb et al. 2018). Also, potential deviations for the mean velocities of up to 2% of U_e were approximated.

The timing of the PIV system was controlled via a Programmable Timing Unit PTU X of LaVision. The triggering was coupled to the wind tunnel data acquisition. The laser pulse timing between two images was set to nominally $\Delta t_p = 250$ ns. A few tests were performed with nominally $\Delta t_p = 150$ ns and $\Delta t_p = 350$ ns to enable random noise and turbulence intensity characterization according to Scharnowski et al. (2019). This resulted in a mean pixel shift of $\Delta x \approx 15$, 26, 36 pixel for $\Delta t_p = 150$ ns, 250 ns, 350 ns, respectively.

Approximately 1500 valid PIV images were recorded per camera for each run with LaVision DaVis 10.2.1. For post−processing, the raw images were de−warped and shift / vibration corrected. Finally, a moving average over three subsequent images was used to reduce background influences. Surface reflections were typically limited to near

wall regions so that a wall distance below approximately 0.1 mm was masked in the recorded images. Velocity vectors were derived using a multi−grid approach with integer window shift to result in an initial displacement field. After that, the velocity field is refined using an iterative predictor–corrector scheme with subpixel accurate image deformation according to the procedure described by Astarita and Cardone (2005). The final corrector step is applied with a Gaussian sub−pixel peak estimator. Typically, for the multi−grid approach two coarsening steps were applied, i.e., a final interrogation window (IW) size of 64×64 pix^2 or 512×16 pix^2 started at 256×256 pix^2 or 2048×64 pix^2, respectively. If not otherwise noted an overlap of 50% was chosen with some selected examples at 75%. Rectangular and Gaussian window weighting was tested for the iterative PIV evaluation. Between the iterations, outliers in the vector field were detected by different means. A normalized median test (over 5×5 vectors) according to Westerweel and Scarano (2005) was applied. Furthermore, vectors were neglected outside of a nominal displacement range of $-1<\Delta x<33$ pix and $2<\Delta y<2$ pix. Additionally, maximal displacement difference of 4 pix between neighboring vectors were allowed. Outliers were replaced by interpolated values, based on the neighboring values. A total of five steps of the iterative evaluation were performed, resulting in a typical validation rate of over 80% in the final dataset. Proper post−processing and validation reduced the valid snapshot count to approximately 1000 images per camera. Additionally, a final post−processing step was used to filter outliers by excluding vectors which lie outside a band of three times the standard deviation around the median value at each vector position, repeating this step for 10 iterations. If not otherwise noted, experimental data points are plotted in this paper only if a minimum of 90% valid vectors exist at the corresponding position. More details of the methods can be found in Marquardt et al. (2020).

The measurement of velocity fluctuations, or turbulent intensities, is sensitive to the choice of IW size. Choosing the size too small for a given data quality increases the random noise whereas choosing it too large increases the amount of sub−grid filtering. Both influences can compensate each other so that care must be taken for the choice of a proper IW. Both influences were addressed on different IW sizes in this study. Random errors were estimated based on an approach according to Scharnowski et al. (2019) which incorporates tests with different laser pulse timing Δt_P at the same flow conditions. It resulted in random errors of 0.41 ± 0.01 pix, 0.44 ± 0.01 pix and 0.55 ± 0.01 pix for an IW of 64×64 pix^2, 48×48 pix^2 and 512×16 pix^2, respectively. The corresponding inner scaled dimensions were $r^+\approx$ 30 x 30, 22 x 22, 237 x 7. For the nominal setup with $\Delta t_\mathrm{p}=250$ ns this translated into 1.6%, 1.7% and 2.2% of U_e, respectively. Additionally, this method gives an estimate for the inflow turbulence intensity, which resulted in a value of $Tu=0.8\pm0.1$%, which is well within the expected range for H2K tests which were measured previously to approximately $Tu=0.83\pm0.11$% (95% CI) from Laser 2 Focus measurements (Gülhan et al. 2021). Sub−grid filtering was estimated based on the work by Lee et al. (2016). The authors derived a database for the attenuation of streamwise and wall−normal Reynolds stress, which uses as input a filter volume, defined by inner−scaled interrogation window size and laser sheet thickness. The reference DNS data are an incompressible turbulent boundary layer at $Re_\tau=1500$ ($Re_\theta=5000$) according to Sillero et al. (2013). The sub−grid filtering analysis for the current work was performed for different IW sizes and a laser light sheet thickness of 1 mm. Unfortunately, the database is limited to a streamwise interrogation window size which corresponds to 215 pix in the current H2K scaling. Therefore, a window of 215×16 pix^2 was used to estimate the Reynolds stress attenuation for the 512×16 pix^2 PIV IW. The real attenuation is most likely larger than the calculated one. To extract a percentage attenuation, also a reference dataset is necessary, which is at best comparable to the data of interest. Here, as reference, the $Ma=4.97$ turbulent boundary layer DNS data according to Duan et al. (2010) (case M5T4: $Ma_\mathrm{e}=4.97, T_w/T_r=0.68, Re_\theta=3819$, $Re_{\delta2}=1526$, $Re_\tau=434$) and Zhang et al. (2018) (case M 6 T w 0 7 6 : $Ma_e=5.86, T_w/T_r=0.76, \mathrm{Re}_\theta=9455$, $\mathrm{Re}_{\delta2}=1746$, $\mathrm{Re}_\tau=453$) were used. For this approximation, inner scaling of the reference data wall−normal distance and Morkovin's scaling of the Reynolds stress were applied. The resulting level of streamwise attenuation at a representative wall−normal distance of $y/\delta=0.5$ is in the order of approximately 10% for all IWs in this work with 8.5%, 7.6% and 10.7% for an IW of 64×64 pix^2, 48×48 pix^2 and 512×16 pix^2, respectively.

Based on the above analysis, the 64×64 pix^2 were chosen as nominal IW size due to a good tradeoff between random errors and filtering. If not otherwise noted, most of the following analyses were performed on data with this IW size with some selected ones on stretched, high aspect ratio, 512×16 pix^2 windows. These latter IWs were used to increase the wall−normal resolution and at the same time ensure an acceptable number of particles per IW. This increased resolution leveraged the extraction of EQSR, where data points of the mean velocity down to the logarithmic region are beneficial. Comparisons of the mean velocity profiles for different IWs showed only negligible differences, except for the corresponding wall−nearest point. Also, previous investigations on synthetic and experimental data showed acceptable results with comparable IWs (Neeb et al. 2018).

The total estimated uncertainty of mean velocities with 95% confidence interval were derived by propagation of

influences from the typical set−up and analysis, calibration quality and laser pulse timing influences as well as averaging over the available instantaneous velocity vectors (based on the work of Benedict and Gould 1996) and resulted in $U_U = 9.9$ m/s or $U_U = \pm 1.1\%$ based on the reference Taylor−Maccoll edge velocity of $U_e = 926$ m/s. The sampling uncertainties for the turbulent fluctuations, e.g., $U_{u'u'}$, were derived by a re−sampling algorithm via the bootstrap method according to Benedict and Gould (1996). The resulting uncertainties are directly given in the corresponding graphs in the results section. The uncertainties of the values in scaled form were derived by typical propagation and are stated in the corresponding sections.

Due to the choice for PEEK as wind tunnel model with its low thermal conductivity, the wall temperature changed during a wind tunnel run by approximately 3–10%, corresponding to a viscosity change of approximately 2–9%.The corresponding impact on the velocity measurements were approximated based on numerical simulations, described in Neeb et al. (2018). For wall−normal distances corresponding to the logarithmic layer or larger, the difference is in the order of $\Delta U/U \approx 0.02\%$ and was therefore neglected.

For the discussion of velocity and turbulence profiles, data along the smooth and rough wall was averaged along a streamwise region, which corresponds to the extent of one roughness shape wavelength ($\lambda = 4k \approx 2\delta$). Along the roughness topology, this averaging window is aligned with the beginning at the downstream end of one roughness crest to the next (i.e., at MS1: $x = 496$–498 mm and at MS2: $x = 626$–628 mm). Different averaging alignments and also extents (i.e., two or four wavelengths) were tested with only negligible differences between the results.

2.2.5 Post−processing for skin friction velocity approximation

Inner scaling is necessary to enable specific types of comparison with theory and also to extract the EQSR. Since no direct measurements of the skin friction velocity were performed, different indirect approaches were utilized. First, a fitting procedure based on the law of the wall was used. Second, a modified integral method to approximate the compressible wall skin friction along the cone model was applied. Both methods were previously used on smooth wall cone flow data and compared favorably to theoretical and numerical predictions (Neeb et al. 2018). In this work, the methods were extended to rough wall flows.

2.3 Fitting approach

For the fitting approach, the parameters of the incompressible law of the wall are modified to match a measured mean velocity profile. In addition to the logarithmic part, the wake part was also included using a proper wake formulation, which can be given e.g., according to Jiménez (2004) with:

$$U^+_{eff} = \frac{U_{eff}}{u_\tau} = \frac{1}{\kappa} ln\left(y^+\right) + B - \Delta U^+_{eff} + \frac{\Pi}{\kappa} W\left(\frac{y}{\delta}\right) \tag{1}$$

In compressible flow, inner scaled coordinates are defined with the wall parameters according to $y^+ = y u_\tau / \nu_w$ with $y = \left(y_T + \epsilon\right)$ including the wall−normal coordinate with the origin at the crest of the roughness elements y_T and the shift of origin ϵ (see also Fig. 2). Additionally, a proper transformation from compressible to an effective incompressible velocity profile U_{eff} is necessary, so that in Eq. (1) the left side becomes U^+_{eff} and on the right side ΔU^+_{eff}. For this transformation different formulations are possible. The most widespread used is the van Driest transformation (see e.g., (Berg 1977; Driest 2003)). Although this transformation has proven to be accurate on multiple data sets for flows along adiabatic walls, more recently, different other transformations have been proposed to include the effect of heat flux, e.g., (Patel et al. 2015; Trettel and Larsson 2016). Since the profiles in this work are close to adiabatic with $T_w/T_{aw} > 0.8$, the van Driest transformation was applied (see also discussions in Neeb et al. (2018)). Equation (1) also contains the Karman constant κ, the law of the wall constant B, Coles wake strength parameter Π (the latter usually depending on inflow and pressure gradient), a wake function W and $\delta = \left(\delta_T + \epsilon\right)$ with δ_T as the boundary layer thickness from the crest of the roughness elements. There are different options for the formulation of the wake function. We used the formulation according to Coles with $W = 2sin^2\left(\frac{\pi}{2}\frac{y}{\delta}\right)$. Including the wake formulation increased the amount of useful data points within the boundary layer, which in turn enhanced the quality of the fitting procedure.

In case of a smooth wall $\epsilon = 0$ and $\Delta U^+_{eff} = 0$, so that Eq. (1) reduces to the classical smooth wall law of the wall. In this case, only u_τ and Π need to be fitted, which is typically a stable procedure. The general problem of applying a fitting procedure in case of a rough TBL profile is the number of free parameters. Usually, the parameters $\Delta U^+, u_\tau, \epsilon, \Pi$ need to be found simultaneously, which makes the fitting procedure very unstable (Berg 1977). Further discussion is included in the result section.

2.4 Integral approach

This method is based on an approach originally implemented to approximate the shear stress along a rough flat plate according to Latin and Bowersox (2000). For this approach, the von−Karman momentum integral equation is solved in between two consecutive positions along the surface. At these positions the momentum loss thickness is extracted from experimentally derived velocity profiles and additionally a functional dependence for the skin friction coefficient of the kind $c_{f,e} = f(\theta)$ is used. This skin friction function can be derived from the law of the wall (Eq. (1)) formulated at the boundary layer edge, or, in case of a fully rough wall, also the formulation according to Jiménez (2004) can be used. In both cases, it needs to be assumed that $\theta/\delta \approx const.$ which can be shown to be acceptable for the condition of interest and within the region of interest with an error of below 1%, based on CFD data. In case of a compressible smooth and rough cone flow, an analytical solution of the resulting formulation is not possible and it needs to be solved numerically. As input, the experimentally derived θ at measurement section MS1 and MS2 is used, besides other edge condition parameters (see Table 2). The procedure was tested and validated with numerical data along a cone and the resulting percentage deviations of the skin friction coefficient was typically $|\Delta c_{f,e}| \leq 1.2\%$ (Neeb et al. 2018). The impact of PIV resolution was estimated with artificially under resolved profile data from CFD to result in typically $|\Delta c_{f,e}| \leq 6\%$.

Table 1 Nominal inflow conditions

State	Ma [−]	Re [10^6 1/m]	p_0 [bar]	T_0 [K]	U [m/s]
Inflow	6.06	15.7	20.0	500	923
Edge	5.40	20.5	19.8	500	920

3 Results

The following section outlines the results of the boundary layer analyses. First, general information is given with an overview of nominal flow conditions and valid runs. Then, general flow features and profiles are discussed based on the mean flow data from PIV. After that, turbulent data are analyzed.

Table 1 contains parameters defining the nominal inflow condition with the reservoir pressure p_0 and temperature T_0, the Mach number Ma, velocity U and Reynolds number Re, both at inflow (condition at nozzle exit, upstream the bow shock in front of the cone) and boundary layer edge (downstream the bow shock). All tests were performed at an angle of attack of zero. Table 2 contains an overview of valid runs with the run number, the measurement section (MS), the wall conditions, the edge Mach number Ma_e and velocity U_e, the wall temperature T_w, the wall to adiabatic temperature ratio T_w/T_{aw} (with estimated $T_{aw} = T_e\left(1 + Pr^{1/3}Ma_e^2(\gamma - 1)/2\right)$ and $Pr = 0.72$), the boundary layer thickness δ, the momentum loss thickness θ and the Reynolds numbers $Re_\theta = \rho_e U_e \theta/\mu_e$, $Re_{\delta 2} = \rho_e U_e \theta/\mu_w$, $Re_\tau = \delta^+ = \rho_w u_\tau \delta/\mu_w$ and $Re_\tau^* = \rho_e \sqrt{\rho_w/\rho_e} u_\tau \delta/\mu_e$. The latter is the semi−local Reynolds number which was suggested for comparing wall turbulence statistics between cases with substantially different mean density and viscosity profiles according to Patel et al. (2015). To derive the momentum loss thickness θ, the mean density profiles for the Morkovin scaling were derived assuming a Crocco–Busemann temperature distribution within the boundary layer (see e.g., White and Corfield 2006) together with the measured surface pressure from the closest tap on the model. Other temperature distributions (e.g., Walz (Duan et al. 2010)) have been tested and only negligible differences were encountered.

3.1 Flow field

The mean flow field along the smooth and rough wall from PIV is shown in the upper part of Fig. 4a and b, respectively. The streamwise and wall−normal distance were normalized

Table 2 Overview of runs performed

Run	MS	Wall	Ma_e [−]	U_e [m/s]	T_w [K]	T_w/T_{aw} [−]	δ [mm]	θ [mm]	Re_θ [−]	$Re_{\delta 2}$ [−]	Re_τ [−]	Re_τ^* [−]
14	1	Smooth	5.1	923	368	0.80	3.6	0.17	3105	807	215	1763
16	1	Smooth	4.9	920	374	0.81	3.6	0.17	2770	763	212	1596
06	1	Rough	4.9	913	368	0.81	4.3	0.21	3426	954	328	2426
07	1	Rough	5.1	918	379	0.83	4.5	0.21	4044	1027	307	2622
08	1	Rough	5.2	928	377	0.82	4.4	0.20	4832	1201	378	3335
10	1	Rough	5.2	947	385	0.81	4.6	0.21	3797	989	308	2540
19	2	Smooth	5.2	925	372	0.81	4.3	0.20	4106	1056	265	2221
20	2	Rough	4.9	910	357	0.78	5.5	0.29	4468	1288	384	2690

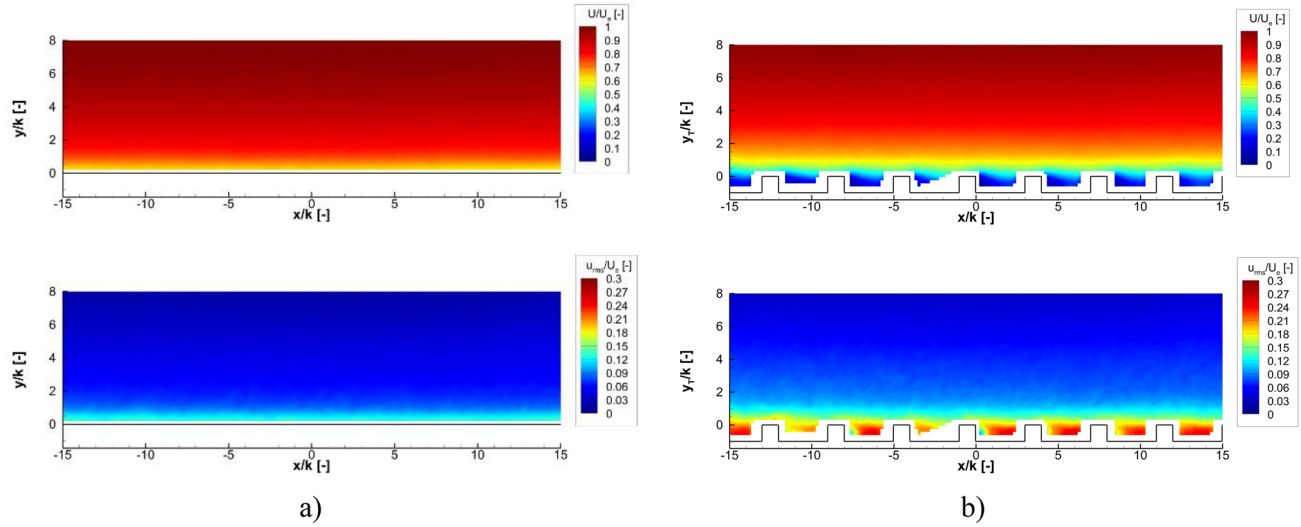

Fig. 4 Mean streamwise velocity U/U_e and streamwise rms velocity u_{rms}/U_e above **a** smooth (Run14) and **b** rough wall (Run07, 48×48 pix^2 with 75% overlap)

with the roughness height. The same scaling was used in case of smooth wall data to be comparable and the origin corresponds to MS1 in both cases. To increase the resolution for visible inspection, IWs of 48×48 pix^2 with 75% overlap were used. The different streamwise velocity layers of the boundary layer which evolve above the walls are clearly visible. The mean boundary layer height is visibly larger in case of the rough wall, with lower velocities at comparable heights. It is visible that the flow is skimming along the roughness elements, with only minor disturbance of the layered structure. Downstream of each roughness trough, shear layers are evolving which are visible by slightly increasing velocities toward the wall near the downstream end of the cavities. The scaled streamwise rms velocities show increased values in a layer close to the smooth wall and above the roughness elements in the aforementioned evolving shear layers. Especially in close vicinity of the crests and inside the cavities the highest values are encountered.

3.2 Mean flow data

3.2.1 Profiles

To further analyze the data, velocity profiles were extracted from the dataset, averaged as described in the Sect. 2 on IW with dimensions 512×16 pix^2. Figure 5 shows profiles at MS1 (solid lines, Run14 and Run07 along smooth and rough wall, respectively) and MS2 (dashed−dotted lines, Run19 and Run20 along smooth and rough wall, respectively) along the smooth (black lines, symbols) and rough wall (red lines, symbols). The typical flow retardation due to the rough surface is clearly visible. Also visible, but only moderately, is the change in profile due to the increased running length (e.g., rough MS1 vs. rough MS2). The run−to−run repeatability is very good (not shown here).

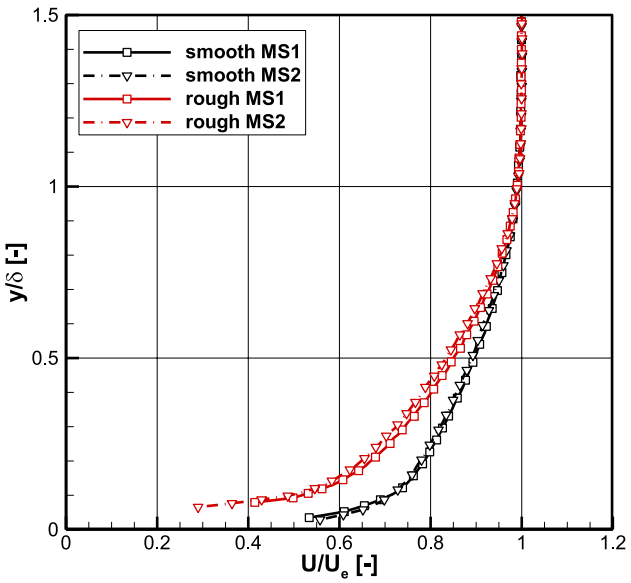

Fig. 5 Outer scaled mean velocity profiles showing the effect of smooth (black lines/symbols, Run14 and Run19 at MS1 and MS2, respectively) and rough wall (red lines/symbols, Run07 and Run20 at MS1 and MS2, respectively)

3.2.2 Inner scaling

By fitting the necessary parameters (see Sect. 2), the inner scaled mean velocity profiles can be compared to the

Table 3 Overview of results from fitting approach

Run	MS	Wall	c_f [−]	u_τ [m/s]	Π [−]	ΔU^+_{eff} [−]	ϵ [mm]	k_s/k [−]	k/δ [−]	k^+ [−]	k^+_s[−]
14	1	Smooth	1.38E−03	51.8	0.41	0	0	0	0	0	0
16	1	Smooth	1.48E−03	52.0	0.40	0	0	0	0	0	0
06	1	Rough	2.45E−03	66.0	0.58	6.34	0.25	1.35	0.12	37.9	51.1
07	1	Rough	1.92E−03	61.7	0.76	5.62	0.25	1.12	0.11	34.2	38.4
08	1	Rough	1.95E−03	63.6	0.72	6.29	0.25	1.16	0.12	34.3	50.2
10	1	Rough	1.52E−03	69.1	0.77	5.70	0.25	1.19	0.11	33.3	39.7
19	2	Smooth	1.24E−03	49.6	0.47	0	0	0	0	0	0
20	2	Rough	1.99E−03	58.1	0.83	6.15	0.25	1.35	0.10	35.0	47.4

classical law of the wall. The law of the wall constant and the Karman constant were chosen to $B = 5.0$ and $\kappa = 0.4$, respectively (see e.g., Berg 1977). The resulting values for all valid runs are summarized in Table 3.

Before being applied to rough profiles, both, the fitting and integral, approaches were tested on the smooth wall data. At MS1 the Run14 data resulted in $u_\tau = 51.8 \pm 0.8$ and 47.8 ± 6.9 m/s for the fitting and integral approach, respectively. Values from the integral approach typically give slightly lower values due to undersampled velocity data in the near wall region. This is accounted for in the uncertainty analysis and both methods agree within their corresponding uncertainties. The values do also agree with the values of the previous smooth wall campaign and prediction from CFD and theory within the corresponding uncertainties (Neeb et al. 2018).

For the rough wall data, the fitting is much more tedious, as previously mentioned. One parameter which was found to have sizeable impact in case of the current data is the shift of origin ϵ. There is a multitude of different approaches to extract this parameter (see e.g., Chung et al. 2021). Different approaches were tested but showed large scatter without a converging answer. Therefore, a different approach was used, described in the following.

First, a value for the rough wall skin friction velocity u_τ is calculated via the integral approach (see Sect. 2) utilizing the momentum loss thickness θ of the PIV velocity profiles at MS1 (Run07) and MS2 (Run20) as input to solve the von Karman integral. With the corresponding uncertainty band, a most likely value band of u_τ was found with $53.4\,\text{m/s} < u_\tau < 71.8\,\text{m/s}$. Then, the fitting approach was applied multiple times, each time with a fixed shift of origin varied in between 0 to 1 k in steps of 0.1 k. This ensured that the origin is located between the floor and the crest of the roughness elements, which is an acceptable value range from previous investigations (Berg 1977; Bettermann 1966; Liu et al. 1966). Figure 6a, b show the results from the fitting procedures for selected rough wall runs with the resulting skin friction velocity u_τ and the roughness function ΔU^+_{eff} against normalized shift of origin ϵ/k, respectively. The blue and red dashed line highlight the aforementioned most likely value corridor from the integral approach. From the results, a most likely value range of $\epsilon = 0.4 - 0.5k$ was extracted and a final value of $\epsilon = 0.5k$ was chosen, to be consistent with previous investigations (e.g., Berg 1977). The resulting fitting parameters are summarized in Table 3. Besides this result, it is emphasized how much influence ϵ has under the current conditions (most probably due to the moderate value for k/δ) and it underlines the importance of a proper choice for the shift of origin.

The resulting roughness function ΔU^+_{eff} was also independently checked with the so−called diagnostic plot approach, which utilizes the ratio of streamwise turbulence to mean velocity profile. This scaling also collapsed the data of this paper onto theoretical correlations, if a roughness scaling according to Castro et al. (2013) was used (not shown here).

Figure 7 a) shows inner scaled van Driest transformed mean velocity profiles along the smooth (black, gray) and rough wall (colored) together with the law of the wall. Additionally, DNS data from Zhang et al. (2018) at comparable conditions are included. All smooth data collapse and follow the law of the wall in the mid− part of the semi−logarithmic plot ($20 \lesssim y^+ \lesssim 70$). Corresponding to the larger Reynolds number, the profile at MS2 results at a larger y^+ at the edge of the boundary layer. Also, the wake is more pronounced for the higher Reynolds number MS2 profiles. Both, the Coles wake parameter Π (see Table 3) as well as the corresponding scaled velocity shift due to the wake with $\Delta U^+_{eff,wake} = 2\Pi/\kappa \approx 2 - 2.4$ shows the expected value range and trend with Reynolds number $Re_{\delta 2}$ for turbulent boundary layers as suggested by Fernholz and Finley (1980). The rough wall profiles show the typical shift by ΔU^+_{eff} below the smooth wall profiles. As reference, a log−law line shifted by $\Delta U^+_{eff} = 6$ is shown in Fig. 7 a), which is the order of magnitude derived from all profiles (see Table 3). The resulting roughness Reynolds numbers k^+ are in a range of 34 to 38. Previous experimental investigations of incompressible flow along transverse bars with $\lambda/k = 3.8$ ($w/k = 0.75$) showed a value of $k^+ \approx 10$ ($\Delta U^+ \approx 5.5$) to be sufficient for a fully rough TBL according to Bandyopadhyay (1987) (see also Fig. 7b). Incompressible TBL DNS data along transverse square bars with $\lambda/k = 7 - 120$ showed a value of $k^+ \approx 19$ ($\Delta U^+ \approx 7.5$) to be sufficient for a fully rough flow according to Choi (2021). Also, Berg

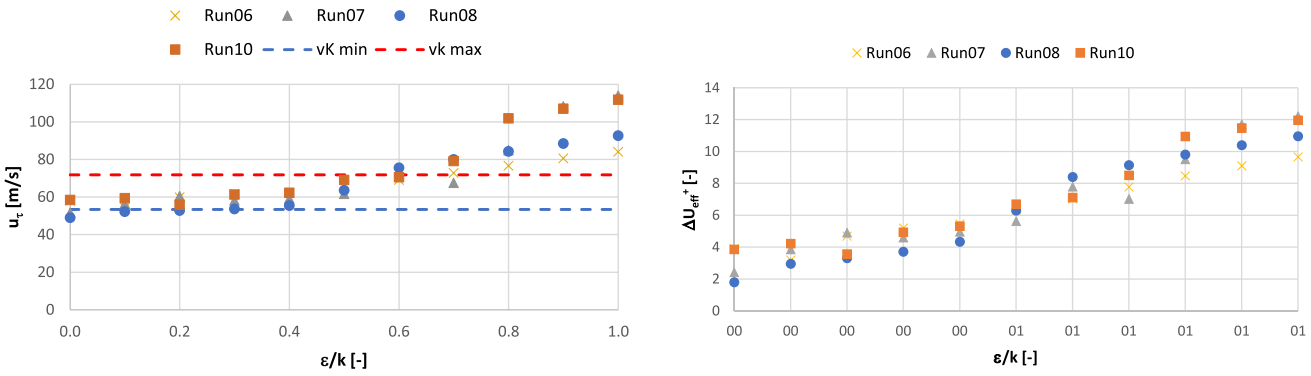

a) b)

Fig. 6 Rough wall skin friction velocity u_τ in (**a**) and roughness function ΔU^+_{eff} in (**b**) from fitting approach against shift of origin ϵ/k for selected rough wall runs. Dashed lines in (**a**) indicate corresponding value range from integral approach including uncertainties

(1977) assumed his compressible data along the transverse square bars with $\lambda/k = 4$ at $k^+ \approx 33.8$ ($\Delta U^+ \approx 6.5$) to be in the fully rough regime. Presuming the TBL data of this work to be fully rough as well, an equivalent sand grain roughness can be found via $k_s^+ = e^{0.4(3.5+\Delta U^+)}$ (with the values for $\kappa = 0.4$ and $B = 5.5$ according to Nikuradse (1933)), which result in approximately $k_s{}^+$=38–59. This would result in $k_s/k = 1.1 - 1.4$, which is closer to the compressible value by Berg than the incompressible investigations. But it needs to be mentioned that in our case as well as Berg's data ($k_s^+ = 44$) the derived k_s^+ values are slightly below the fully rough limit, typically given with $k_s^+ = 60 - 70$, and therefore transitional roughness effects cannot be excluded completely and the derived k_s/k values need to be taken with some caution.

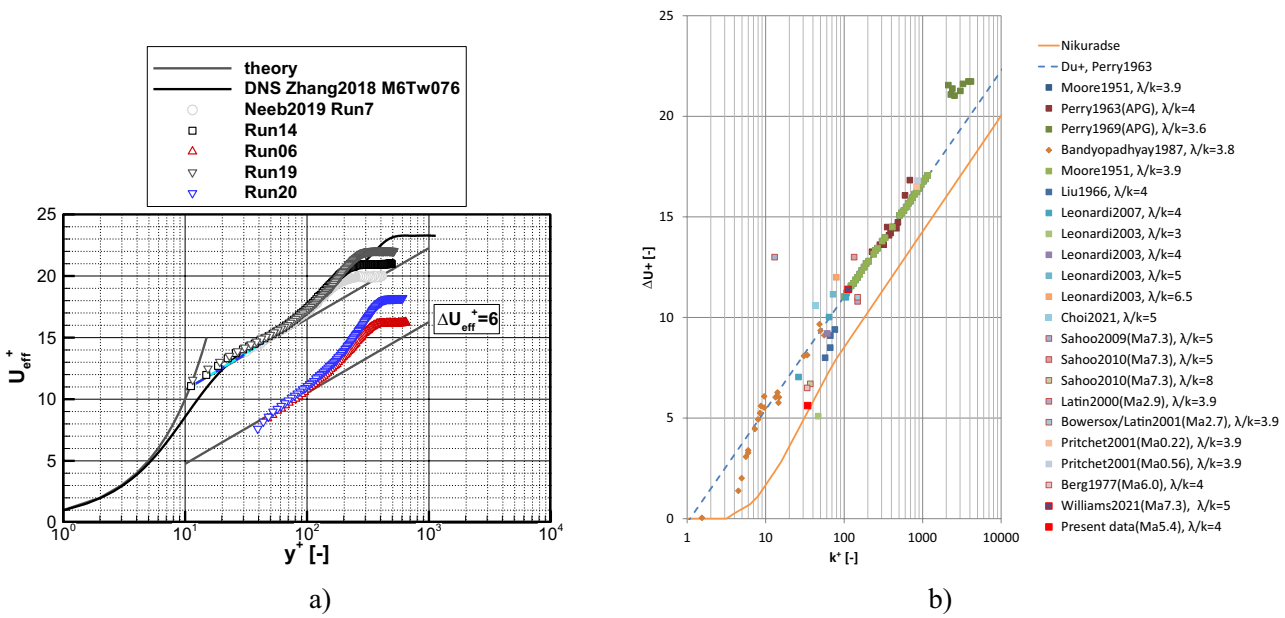

a) b)

Fig. 7 **a** Inner scaled van Driest transformed mean velocity profiles along smooth (black, gray) and rough wall (colored) together with the law of the wall and DNS data according to Zhang et al. 2018. **b** Roughness function ΔU^+ against roughness Reynolds number k^+ for square bars of different wavelength close to a value of $\lambda/k = 4$ and authors (symbols without and with edge for incompressible and supersonic data, respectively) according to Nikuradse (1933), Berg (1977), Perry and Joubert (1963), Liu et al. (1966), Latin and Bowersox (2000), Sahoo et al. (2010), Sahoo et al. (2009), Williams et al. (2021), Pritchett and Bowersox (2001), Choi (2021), Moore (1951), Perry et al. (1969), Leonardi et al. (2007), Leonardi et al. (2003), Choi et al. (2020), Bowersox and Latin (2001)

The above-stated approach gives a best estimate based on the previous choice for ϵ. Due to the range of acceptable u_τ based on the uncertainties from the integral approach, also the fitting parameters can vary in certain value range. For example at MS1 (results from four different runs), the accepted range of u_τ between 53.7 and 70.5 would result in ΔU^+_{eff} to vary from 3.2 to 7.1, therefore k^+ from 34.2 to 37.1, k_s^+ from 14.5 to 69.5 and finally k_s/k from 0.4 to 1.9. This highlights the sensitivity of the analysis, although based on state−of−the−art measurement techniques. This is not necessarily only due to the additional challenges posed by the compressible flow, but can also be seen in incompressible investigations, visible by the large scatter of derived EQSR from different investigators as given in the Introduction.

Apart from that, rough wall profiles show in general larger wake parameters up to approximately 0.8 (see Table 3), similar to previous studies e.g., (Krogstad et al. 1992; Perry and Li 1990; Castro 2007). There is ongoing debate if true smooth and rough wall boundary layer universality exists, for which the same wake parameter value range would be expected and different parameters are discussed to have an impact (Castro et al. 2013). For outer similarity to hold, Coles wake parameter is expected to agree between smooth and rough wall flows. We continue the discussion about smooth to rough profile similarity based on turbulence data in the following sections.

3.3 Turbulent data

In this section, streamwise velocity fluctuations are discussed in context of literature data and the effect of roughness. After that, two−point correlations of the velocity fields and the presence of uniform momentum zones are analyzed to investigate the structure of the TBL along the smooth and rough wall.

3.3.1 Profiles

Streamwise velocity fluctuations were extracted from the PIV data. Smooth wall results are shown in Fig. 8 in outer Morkovin scaling, utilizing $u_* = \sqrt{\rho/\rho_w}u_\tau$, in comparison to CFD data and other experimental data. The same spatial averaging as for the mean profiles was applied. The error bars represent the sampling uncertainties according to Benedict and Gould (1996) together with uncertainties for values relevant for Morkovin scaling. For comparison, experimental boundary layer data were included with $Ma = 2.86$, $Re_\theta \approx 60000$ data according to Ekoto et al. (2008), $Ma = 7.2$, $Re_\theta \approx 3600$ data according to Sahoo et al. (2009), $Ma = 7.6$, $\text{Re}_\theta = 9337$ data according to Williams and Smits (2017) and incompressible experimental data by Klebanoff (1955) ($\text{Re}_\theta = 6940$). Additionally, DNS data in the plots correspond to Duan et al. 2010, 2011 (in legend M0: $Ma_e = 0.3, T_w/T_r = 1$, $Re_\theta = 15148$, $Re_{\delta 2} = 1515$, $Re_\tau = 570$; M5: $Ma_e = 4.9, T_w/T_r = 1$, $Re_\theta = 4932$, $Re_{\delta 2} = 1587$, $Re_\tau = 417$; M5T4: $Ma_e = 4.97, T_w/T_r = 0.68, Re_\theta = 3819, Re_{\delta 2} = 1526$, $Re_\tau = 434$; M5T5: $Ma_e = 4.97, T_w/T_r = 1$, $Re_\theta = 4841$, $Re_{\delta 2} = 1537, Re_\tau = 386$) and Zhang et al. (2018).

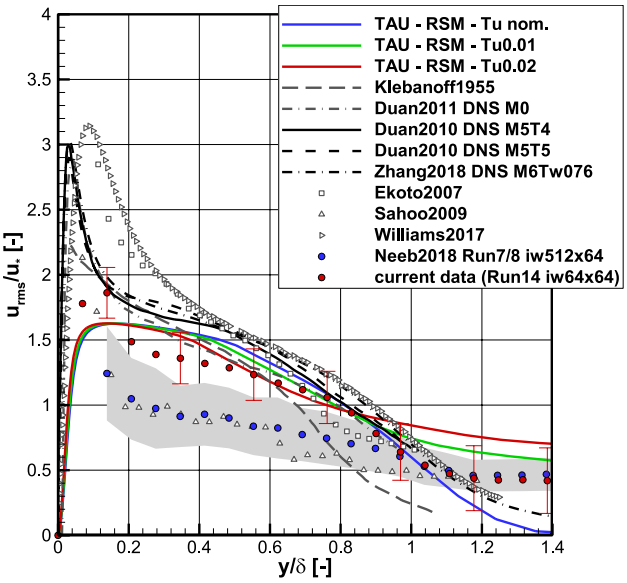

Fig. 8 Profiles of outer layer Morkovin scaled streamwise velocity fluctuation component in comparison to previous experimental (Ekoto et al. 2008; Sahoo et al. 2009; Williams and Smits 2017; Klebanoff 1955) and CFD data (Duan et al. 2010, 2011; Zhang et al. 2018)

The PIV data of the streamwise Reynolds stress (red symbols in Fig. 8) correspond in a large portion of the upper boundary layer well to CFD data from DNS and TAU. At the boundary layer edge, the streamwise Reynolds stress suggests a value close to, but slightly below the TAU computation with an inflow turbulence level of 1%, which corresponds well to the previously derived value of 0.8% in Sect. 2 and also to previous investigations in the same facility, also shown here with blue circles together with corresponding uncertainty bands as gray areas (Neeb et al. 2018). In the vicinity of the turbulence peak from DNS ($y/\delta = 0.03 - 0.09$, depending on the data set), the current PIV data underpredict the corresponding streamwise Reynolds stress. The data only agree to TAU RANS computations, which are known for their lack of resolving the Reynolds stress peak for hypersonic TBL flow (Wang et al. 2019). This filtering is even more drastically in the other components, namely the wall-normal and Reynolds shear−stress component, comparable to previous high Mach number PIV investigations (not shown here). Known influences are particle response behavior due to the limited Stokes numbers and also sub−grid filtering effects.

Figure 9 shows outer Morkovin scaled turbulence profiles in streamwise direction for smooth and rough wall data together with compressible unfiltered and filtered DNS profiles according to Zhang et al. (2018). The filtered DNS was derived based on the approach by Lee et al. (2016) for the chosen PIV IW size and 1 mm laser sheet thickness (IW 64 × 64 x 128 pix^3) which lead to a visible attenuation below the unfiltered value (gray to black dash−dotted line). A representative smooth wall (Run14) and rough wall run (Run07) are chosen to enable a direct comparison. In general, the streamwise turbulence intensity profiles show run−to−run scatter, where typically all MS1 data agree very well, only the MS2 profiles show some differences in the mid part of the TBL (not shown here). Despite these differences, the plotted experimental data agree to the filtered smooth wall DNS data and also to each other, independent of the wall status, when the corresponding uncertainties are accounted for (error bars). Due to the sub−grid filtering by the corresponding IW dimensions, one could argue that potential differences due to different dominant length scales between smooth and rough wall flows are also masked. However, this correspondence between smooth and rough wall visible in Fig. 9, was independent of the tested IW size, which only had an influence on the overall level of Reynolds stress.

Additionally, two wall normal positions with $y = 5k$ and $y = 3k_s$ are indicated in Fig. 9, which have been used in previous investigations to approximate the height of the roughness sublayer, which is a layer where roughness has

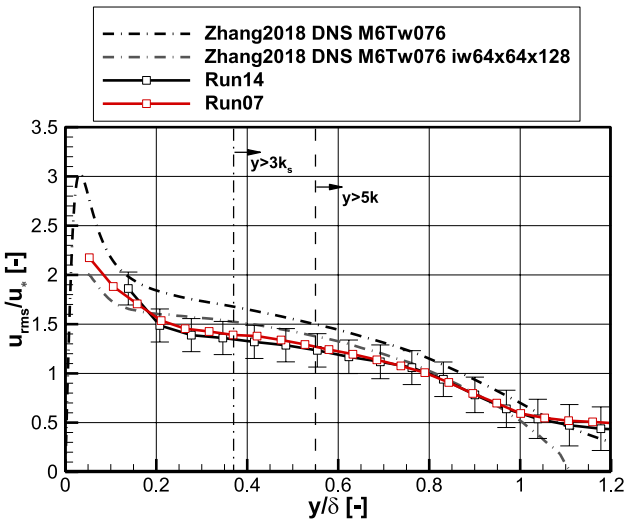

Fig. 9 Turbulence profiles of smooth (black symbols/line) and rough wall (red symbols/line) experiments in outer layer Morkovin scaling in streamwise direction together with compressible unfiltered (black dash−dotted line) and filtered DNS data (gray dash−dotted line) according to Zhang et al. (2018) with filtering approach according to Lee et al. (2016)

a decisive effect on the boundary layer (Chung et al. 2021). According to outer layer similarity (or Townsend's hypothesis), above this sublayer, roughness should have no influence on the outer layer other than defining the boundary conditions like skin friction velocity and boundary layer thickness (Chung et al. 2021). This similarity is thought to exist for sufficiently high Reynolds numbers and scale separation ($\delta \gg k$). Despite the only moderate scale separation in this work, in Fig. 9 it is visible that the streamwise Reynolds stress components agree to within the scatter of the data for the indicated layers, supporting the notion of outer layer similarity. This agreement can also be seen for the other two components of the turbulence intensities, but due to the decisive filtering, these data were excluded for further analysis (not shown here). The agreement is surprising since the mean data would suggest otherwise, due to the difference in Coles wake parameter Π (see Table 3). Additionally, Flack et al. (2007) suggested that even higher Reynolds numbers are necessary for two−dimensional transverse square bars in contrast to three−dimensional roughness like cubes in incompressible flow. Castro et al. (2013) discussed the seemingly contradictory observation of collapsing smooth and rough wall streamwise turbulence profiles whereas the mean profiles show a difference in Coles wake parameter. One stated obvious explanation was that full universality between smooth and rough TBL don't exit. An alternative reason was the general challenge of ensuring that the numerous roughness parameters are sufficiently met, one of the first challenges being that it is not fully known which parameters are actually the most important. He suggested two factors to have major influence with the roughness strength y_0^+ and scale ratio δ^+/y_0^+ instead of the, sometimes equivalently used, parameters k^+ (or k_s^+) and δ/k (e.g., by Jiménez 2004). It can be shown that the alternative forms to quantify the roughness strength with ΔU^+ and y_0^+ are connected via $\Delta U^+ = 1/\kappa \ln\left(y_0^+\right) + B$ (Castro et al. 2013). Castro suggested a necessary parameter range with $y_0^+ \gtrsim 10$ (although $y_0^+ \gtrsim 2$ already corresponds to $k_s^+ \gtrsim 70$) and $\delta^+/y_0^+ \lesssim 300$ to ensure fully rough flow at proper scale separation. In our case $y_0^+ \approx 1.3 - 1.7$ and $\delta^+/y_0^+ \approx 190 - 240$ which are close but fall short of the given boundaries. Therefore, transitional roughness effects cannot be excluded completely.

3.3.2 Two−point correlations

Two−point correlations, as described by Eq. (2), can be exploited to identify the large−scale structures of a TBL as "correlated mass(es) of fluid" (Arnette et al. 1995). Here, correlations of the streamwise velocity fluctuations R_{uu} were analyzed with

$$R_{uu}\left(x,\Delta x,y,y_{ref}\right)=\frac{\overline{u'\left(x,y_{ref}\right)u'(x+\Delta x,y)}}{\sqrt{\overline{u'\left(x,y_{ref}\right)^2}}\sqrt{\overline{u'(x+\Delta x,y)^2}}} \quad (2)$$

Included are the marching step Δx and wall normal coordinate of interest y_{ref}. Figure 10 shows exemplary the two−point correlations of the streamwise velocity fluctuations above a) the smooth and b) the rough wall at y/δ = 0.5. The correlations in Fig. 10 are representative for the orientation and distribution of the TBL large−scale motions. These structures are important in characterizing the distribution of Reynolds stresses because most of the turbulent kinetic energy (TKE) in the boundary layer is contained within long−wavelength motions (Peltier 2013). The correlations are visible as elliptical distributions of R_{uu} with a small rotation angle with respect to the wall. The general appearance of both shapes and orientations of the smooth wall correlations are consistent with previous incompressible studies like Hutchins and Marusic (2007) and supersonic studies like Ganapathisubramani (2007), Peltier (2013) and Williams et al. (2018). The rough wall results are also comparable to previous supersonic studies like Peltier (2013) and Williams et al. (2021). In general, smooth and rough wall correlations look similar in Fig. 10. Details of dimensions and orientations are extracted and discussed in the following. Before analyzing differences to rough wall data, smooth wall results are compared to data from previous investigations.

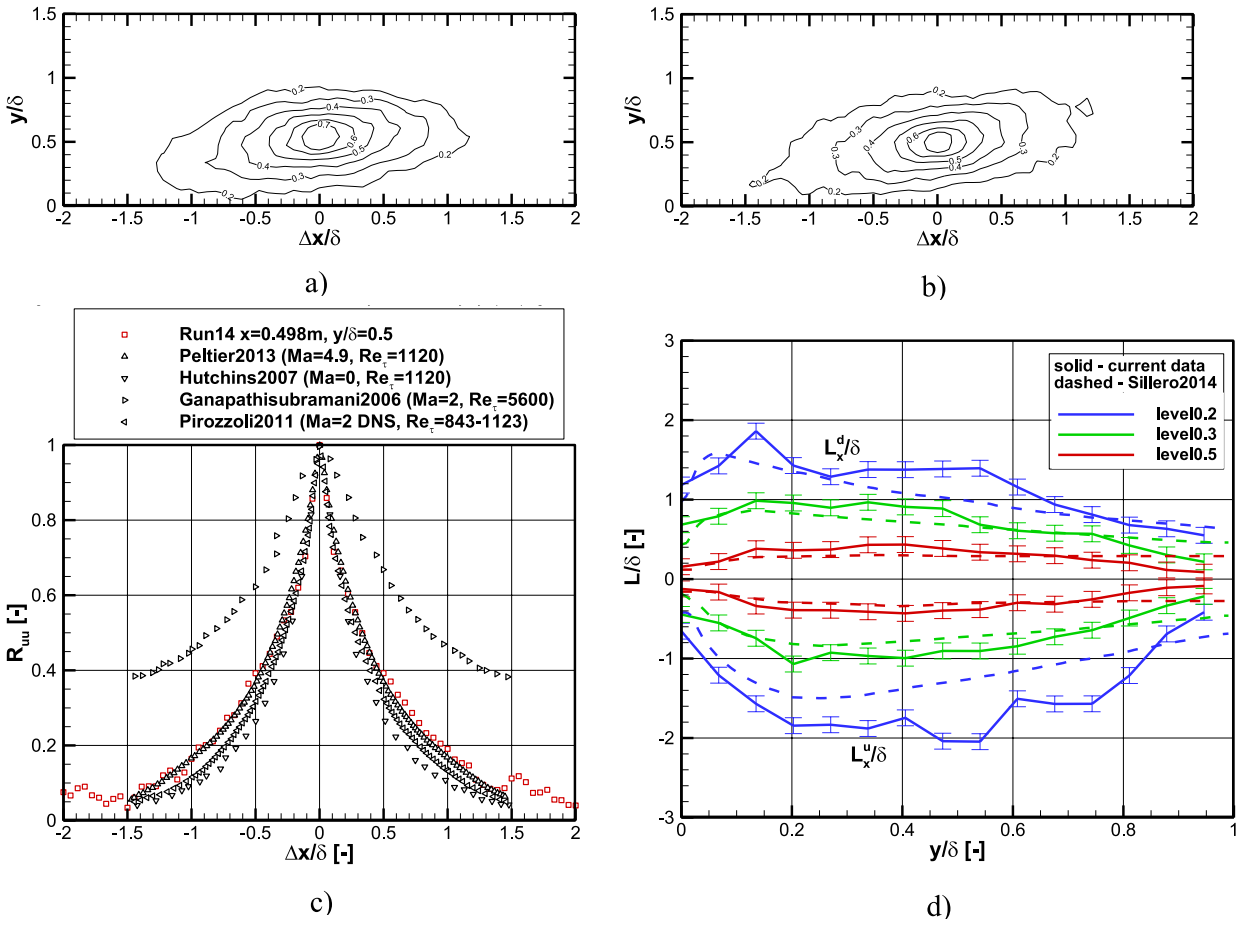

Fig. 10 Two−point correlation results of streamwise velocity fluctuations with (**a**) and (**b**) contour plots at $y/\delta = 0.5$ along smooth (Run14) and rough wall (Run07), respectively, **c** resulting one−dimensional autocorrelation of the streamwise velocity fluctuations $R_{uu}(y_{ref})$ at $y/\delta = 0.5$ for smooth wall (Run14) compared to data from Peltier (2013), Hutchins and Marusic (2007), Ganapathisubramani et al. (2006) and Pirozzoli and Bernardini (2011), (**d**) dimensions of the smooth wall (Run14) correlation contours with wall−normal position represented by the change of upstream, L_x^u, and downstream, L_x^d, extent of different levels (0.2, 0.3 and 0.5) compared to data from Sillero et al. (2014)

To enable direct comparison to previous studies, Fig. 10 c) shows the one−dimensional autocorrelation $R_{uu}(y_{ref})$ extracted at $y/\delta = 0.5$ of the two−point correlation. The autocorrelation of the smooth wall Run14 shows excellent agreement with both incompressible data by Hutchins and Marusic (2007) and compressible data of the $Ma = 2$ DNS study of Pirozzoli and Bernardini (2011) and the experimental data at $Ma = 4.9$ of Peltier (2013). Only data by Ganapathisubramani et al. (2006) seem to indicate larger length scales, which was previously attributed to the corresponding larger Reynolds number (Peltier 2013).

To analyze characterizing length scales, the streamwise dimensions of the two−point correlation contour levels (Fig. 10 a) and b) were extracted. We follow the nomenclature by Sillero et al. (2014) with L_x^u being the upstream and L_x^d the downstream dimension of the corresponding contour level, measured from the point of interest ($x, y_{ref} = 0, 0$, where $R_{uu} = 1$). Figure 10 d) shows the dimensions of the previously defined dimensions for the smooth wall Run14 in comparison to incompressible TBL data of Sillero et al. at $\delta^+ = 2000$ (Sillero et al. 2014). Despite the difference in Mach and Reynolds number, good agreement between hypersonic and incompressible data for contour levels 0.2 and 0.3 can be seen. Uncertainties were conservatively estimated to $U_{L/\delta} \approx \pm 0.1$ (indicated by error bars), based on run−to−run differences and from offsetting the streamwise position for R_{uu} by one IW upstream or downstream. It is visible that the up− and downstream length scales are not symmetrical for both data sets, with a slightly larger downstream leg, especially for level 0.2 and 0.3. Some deviations, especially in the mid part of the TBL ($0.1 < y/\delta < 0.7$), are visible for level 0.2. Close to the boundary layer edge, current length scales tend to fall below the corresponding values by Sillero et al., which might be attributed to the model being a cone or the seeding quality outside the boundary layer.

The difference between smooth and rough wall maximum streamwise dimensions, defined as $L_x^m = |L_x^u| + |L_x^d|$, against wall−normal distance is shown in Fig. 11 for the contour levels from 0.2 to 0.5. The length scales increase with distance to the wall to a maximum at a certain location above the wall and taper−off again toward the edge of the TBL with a tendency to lower length scales with increasing contour level. The length scales are in general very comparable between smooth and rough wall data and clear differences are masked by data scatter and uncertainties. The latter were conservatively estimated to $U_{L/\delta} \approx \pm 0.2$ (indicated by shaded region and bars for the smooth wall and rough wall length scales, respectively). However, for the largest two contour levels $R_{uu} = 0.2$ and 0.3, close to the wall for $y/\delta \lesssim 0.2$, the rough wall values decrease below the smooth ones by approximately 30%. Similar observations were made previously by other investigators. For example Peltier (2013) discovered for their $R_{uu} = 0.4$ contours that close to the wall

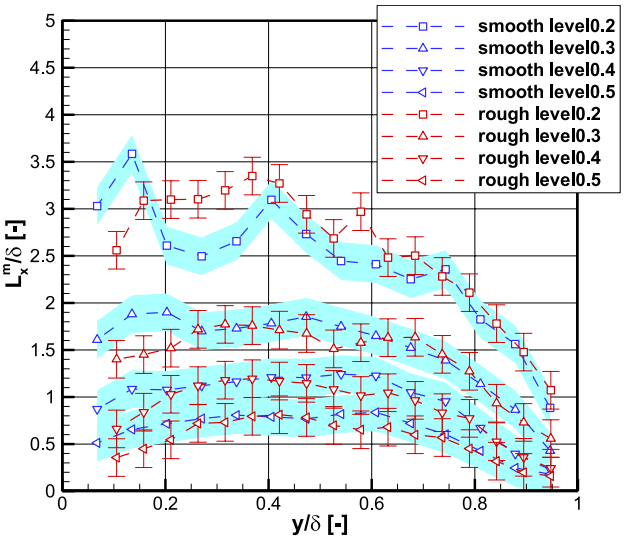

Fig. 11 Wall−normal variation of maximum streamwise dimension L_x^m for two−point correlation contour levels 0.2–0.5 of smooth wall (Run14) and rough wall data (Run07)

with $y/\delta < 0.2$ in a $Ma = 4.9$ flow, the scales along the diamond roughness elements ($k/\delta \approx 0.07, k^+ = 161$) decreased clearly to roughly half the smooth ones. The near rough wall length−scale decrease was also observed by Williams et al. for the 1.27 mm transverse square bar roughness ($k/\delta \approx 0.1$, $k^+ = 70$) compared to reference smooth wall data (Williams et al. 2021). Peltier (2013) connected the near wall behavior to an increase in ejection events via a quadrant analysis of the Reynolds shear stress profiles. If the same analysis is applied to the data of this paper, only negligible differences between smooth and rough wall data are visible for the different quadrants (not shown here). However, the current Reynolds shear stress data and so the quadrant analysis may be influenced by the observed strong filtering.

Another feature of interest is the inclination angle ϕ of the correlation contours, sometimes attributed to the inclination angle of hairpin packets in incompressible TBL (Williams et al. 2018). It can be extracted via the angle of the semi−major axis of an ellipse fitted to the different contour level lines. Figure 12 a) and b) show the extracted inclination angle with wall distance of the smooth (Run14) and rough wall data (Run07), respectively. The symbols show the angles for different contour levels from 0.2 to 0.5. The dashed line represents the mean angle of the corresponding contour levels. The dashed−dotted line corresponds to angles derived via a linear least−square fit through the fitted ellipses of the two−point correlations according to Pirozzoli and Bernardini (2011). It is visible that the angles are in general comparable between the different contour levels and extraction methods, where the second method results locally in slightly smaller angles. Values for $y/\delta \gtrsim 0.8$ are typically

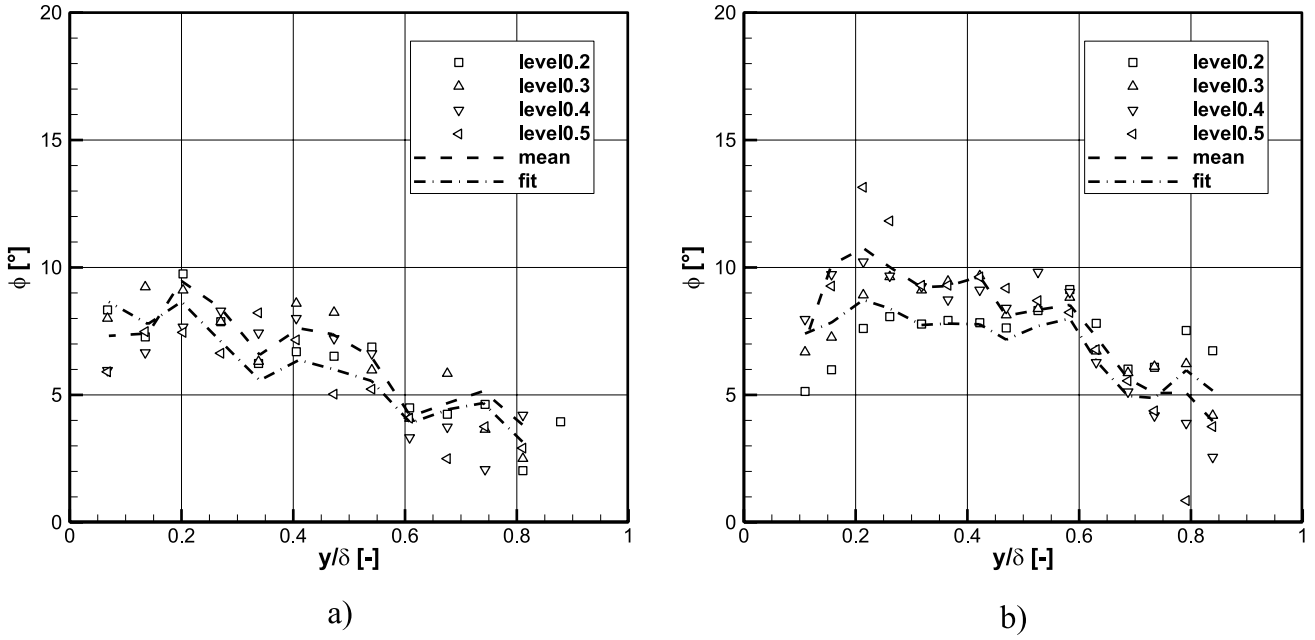

Fig. 12 Inclination angle of the of two−point correlations with wall−normal distance for contour levels between 0.2 and 0.5 for **a** smooth wall (Run14) and **b** rough wall data (Run07). In both plots dashed lines and dashed−dotted lines represent the mean of levels 0.2–0.7 and a linear fit through the fitted ellipses, respectively

blanked, because they tend to be very noisy, again most likely due to the seeding quality. Typically, with increasing distance to the wall, the angles increase to a maximum and taper off again toward the edge of the TBL and are roughly constant over a range of $0.1 < y/\delta < 0.5$. The distribution of angles is comparable between smooth and rough wall data with slightly larger angles in case of the rough wall data for $y/\delta \gtrsim 0.2$, which is the opposite observation reported by Peltier et al. along diamond roughness (Peltier 2013) and Williams et al. along square bar roughness whereas his mesh roughness results showed the same trend (Williams et al. 2021). However, Williams et al. admitted that the small angular differences are difficult to interpret due to strong scatter of the data, which is also the case for the current data.

Figure 13 put representative mean values of the length scale L_x^m and inclination angle θ of this work in context with previous investigations plotted against edge Mach numbers Ma_e. The symbols for L_x^m in Fig. 13 a) typically represent averaged values of the contour level 0.5 in the mid−part of the boundary layer within $0.3 < y/\delta < 0.7$. It is indicated in the legend if other regions are considered for averaging. Bars represent the value variation occurring in the corresponding wall−normal region, if available. Open symbols represent smooth and closed symbols rough wall data.

Typically, values of L_x^m/δ between 0.3 to 0.8 were extracted from data in the current study, well within the range of previous comparable compressible studies, especially according to Peltier et al. derived at a comparable flow condition (Peltier 2013). If only the smooth wall data of this study are considered, values are in a range of L_x^m/δ between 0.6 to 0.8. The slightly larger Reynolds number Run14 shows a larger correlation length than Run16. This would correspond to an expected trend following Smits et al., who suggested that the integral length scale tends to increase with Reynolds number and decrease with Mach number (Smits and Dussauge 2006). In contrast, the value at MS2 (Run19) with an even larger Reynolds number doesn't follow this trend but falls in between the other two smooth wall data points, although it must be pointed out that it also shows a larger scatter. Typically, rough wall data of this study is below the corresponding smooth wall data, also when data spread is considered. Only the rough wall MS2 value (Run20) shows a larger or comparable length scale than the smooth wall data, although this data point was recorded at the largest Reynolds number. In general, the length scale data of this work supports the conclusion by Williams et al., that correlation lengths are only moderately decreasing with Mach number, in contrast to suggested by data which relied on hot−wire measurements, influenced by density (Williams et al. 2018).

The symbols for the inclination angle θ in Fig. 13b represent averaged values of the two−point correlation contour level 0.5 in the mid−part of the boundary layer. Typically, this is within $0.3 < y/\delta < 0.7$, again indicated in the legend if a different region was considered. Our data was extracted within $0.3 < y/\delta < 0.5$ where profiles showed a nearly

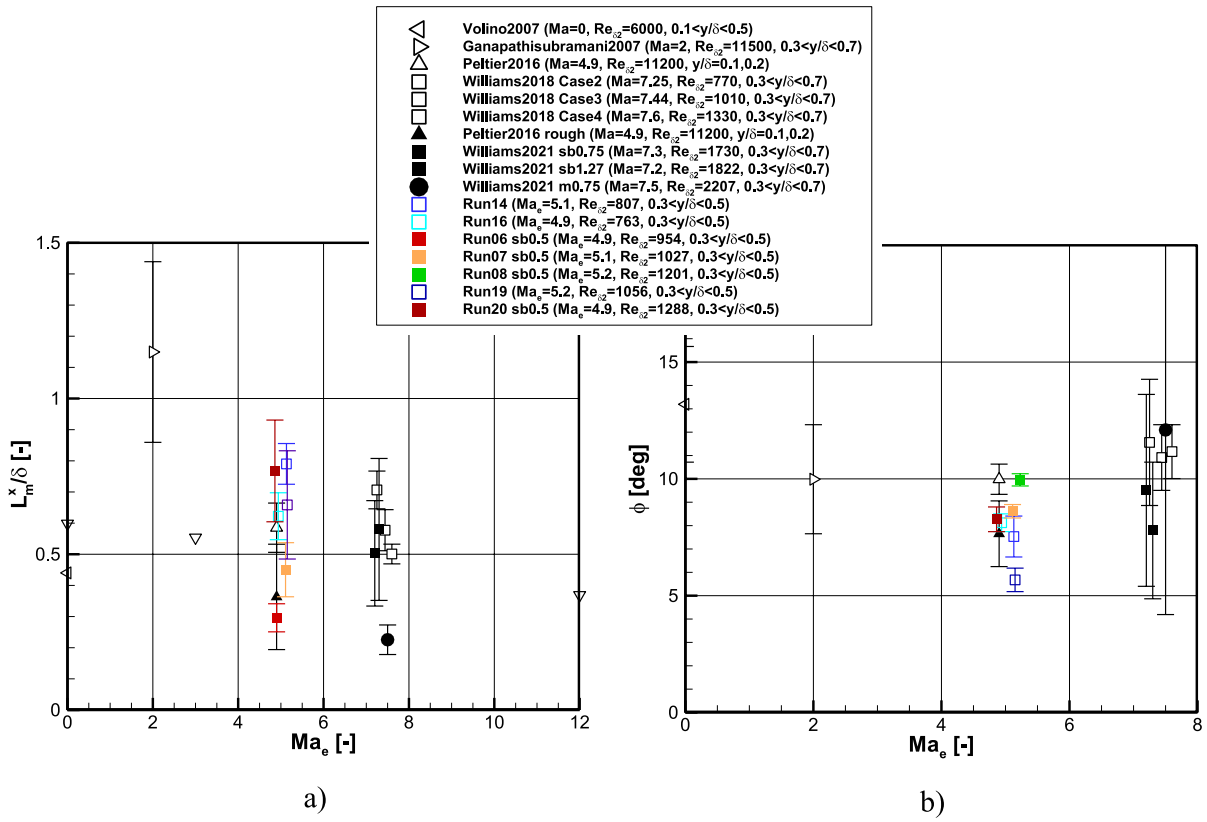

Fig. 13 **a** Averaged max. contour dimension L_x^m against edge Mach number, **b** averaged inclination angle θ against edge Mach number in comparison to literature data as noted in the legend

plateau−like behavior (see Fig. 12), although the smooth wall data show an overall nearly linear trend throughout the boundary layer. In general, our data shows mean values within a range of θ between approximately 6–10°. This is slightly below typical values from incompressible data between approximately 12–16° extracted from estimates of mean log−layer inclination angles, which are thought to be invariant with Reynolds number (Marusic and Heuer 2007). Also, the inclination angle data supports findings by Williams et al., that angles are slightly decreasing with Mach number, in contrast to the reverse trend suggested by data which relied on hot−wire measurements, influenced by density (Williams et al. 2018). The smooth and rough wall data range is in agreement with results from previous comparable compressible studies, especially according to Peltier (2013). Within the scatter of the data, smooth and rough wall data are in agreement, showing no clear tendencies. This would further support the assumption by Townsend, that the outer flow is not drastically affected by roughness.

3.3.3 Uniform momentum zones

In incompressible flows, large, irregularly shaped regions with relatively uniform streamwise momentum, called uniform momentum zones (UMZ), have been observed in several different studies e.g. (Adrian et al. 2000; Silva et al. 2016). Those zones, separated by regions of high shear, have been attributed to the general concept of hairpin vortex structures, where a uniformly retarded flow region in each zone is the backflow induced by several hairpins aligned in a coherent pattern in the streamwise direction (Adrian et al. 2000). In contrast to the term ‘layer’ which is typically used for TBL to distinguish between different regions defined by the mean velocities, for the uniform momentum the term ‘zone’ is used to distinguish that here the instantaneous velocity is of interest. In a previous experimental study, Williams et al. detected UMZ also in a hypersonic TBL along a smooth flat plate (Williams et al. 2018). A numerical study also confirmed this finding in hypersonic TBL according to Cogo et al. (2022). UMZs can generally be detected in instantaneous PIV velocity fields. Figure 14 shows exemplary instantaneous velocity fields for both smooth a) and rough b) wall runs, where UMZs can easily be detected by visual inspection of the occurrence of uniform contour regions (different dashed lines indicate different UMZ boundaries as detected by the p.d.f. approach, as explained in the following). Another way to detect UMZs is to compare instantaneous velocity profiles (red line, here

taken at the middle of the field) to the corresponding mean profiles at the same position (black solid line, based on all images), visible in the upper right of Fig. 14a, b. In the profile plots, the UMZ boundaries are indicated with horizontal dashed lines and the corresponding increased shear is clearly visible by the large local instantaneous velocity differences. Yet another way to detect UMZs is by identifying local maxima in a probability density histogram (p.d.f.) of the velocities according to Silva et al. (2016). Before applying the p.d.f., the velocities outside the boundary layer are excluded via a criterion for the turbulent/non−turbulent interface (TNTI) according to Silva et al. (2013) (also indicated as dashed−dot−dotted lines in the instantaneous velocity contour plots). This p.d.f. is visible in the upper left of Fig. 14a, b with the vertical dashed lines indicating the different UMZ boundaries. The different dash−styles, indicating the different UMZ boundaries in all three subplots, correspond to each other. Figure 14 is only one snapshot in time, but UMZs are abundant throughout the data set (not shown here).

Although easily detectable, a rigorous quantitative analysis for example with respect to the exact amount of UMZs is more challenging. There are open points with respect to the influence of several parameters to be chosen for the analysis. For example, the proper size of the FOV as well as the resolution of the velocity field has a decisive impact on the detection of UMZs. Also, some parameters concerning the resolution and detection of peaks in the velocity histogram have a certain impact. Therefore, no in−depth but an overall statistical analysis is performed with a certain fixed parameter set.

For the IW 64×64 pix^2 data at maximum 2890 instantaneous velocity vectors are available for an analysis of 1487 valid images. A maximum possible streamwise extent of $FOV_x^+ \approx 1200-1400$ was used, which is lower but close to the suggested value of 2000 according to Silva et al. (2016). Via the histogram analysis 2.8 ± 1.1 zones for the smooth Run14 at $Re_\tau\approx220$ can be found. This value does not change drastically for an IW of 48×48 pix^2 with 2.9 ± 1.1 on 5290 instantaneous velocity vectors. The found mean number of UMZs is comparable to the reported value of 2.9 according to Williams et al. (2018) for a smooth wall TBL at $Ma=7.6$, $Re_\tau=279$ and also within range of the reported value of 2.5 UMZs according to Cogo et al. (2022) for a smooth wall TBL at $Ma=5.86$, $Re_\tau=1080$–1953. Previous incompressible studies showed a log−linear dependence of the mean number of UMZs $\overline{N}_{UMZ}$ with Re_τ (Silva et al. 2016). According to this empirical curve, the mean number of zones should lie within $\overline{N}_{UMZ}=[2.0;2.3]$ if a range of Reynolds numbers with $Re_\tau=[200;300]$ is chosen, corresponding to the current study and the one by Williams et al. Therefore, current hypersonic data seem to hint at slightly more zones than predicted from the incompressible correlation, but if the corresponding uncertainties are considered, the numbers still agree. If instead of Re_τ the semi−local Reynolds numbers

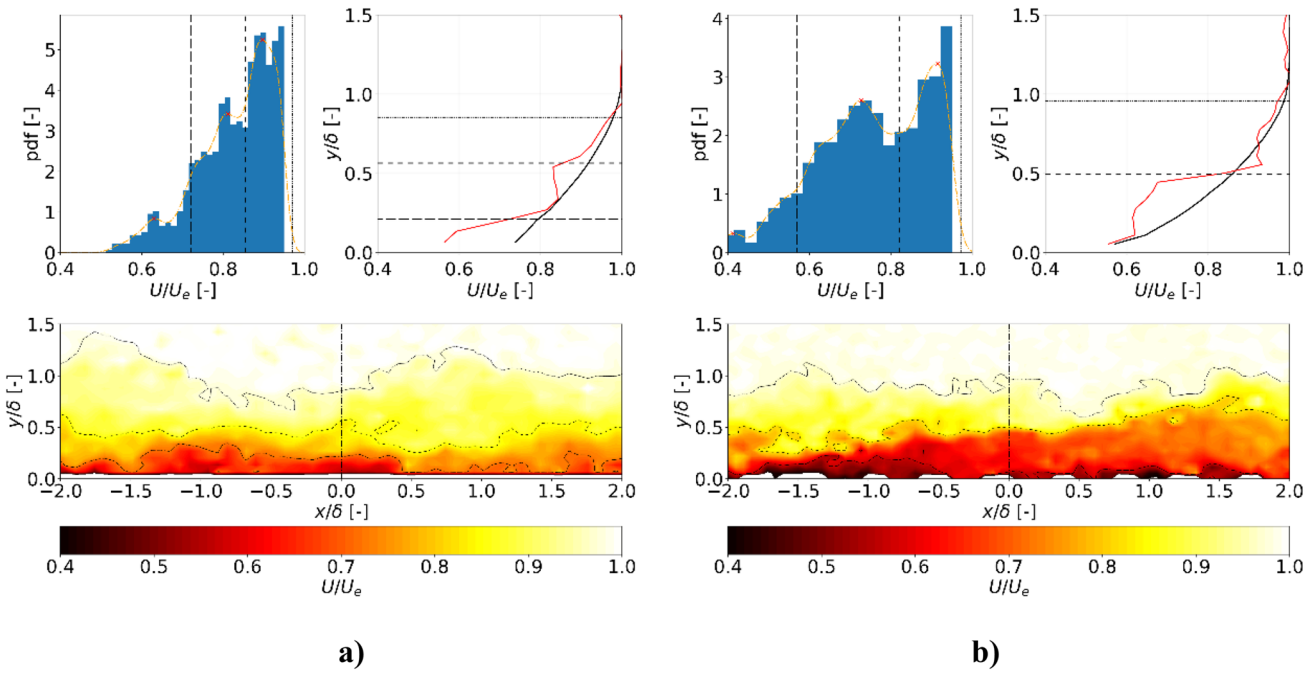

Fig. 14 Compilation of p.d.f. (upper left) based on an instantaneous velocity field (lower middle) and a comparison of an instantaneous (red line) to the mean velocity profile (black line, upper right) for **a** smooth wall (Run14) and **b** rough wall data (Run07). Boundaries for each UMZ are indicated as black lines of different dash−styles which correspond to each other in all corresponding subplots. TNTI is indicated in all subplots as black dash−dot−dotted contour line

were to be used as representative value for the hypersonic data with $Re_\tau^* = [1600;2700]$ (see Table 2), the incompressible correlation would result in $\overline{N}_{UMZ} = [3.5;3.9]$, which gives now much higher values than from the above analysis. It is clear that further analysis is necessary.

If the same approach is used on the rough wall data, values of $\overline{N}_{UMZ} = 2.9 \pm 1.0$ and 2.5 ± 1.0 can be extracted from Run07 and IW 64×64 pix^2 (2890 instantaneous vectors) and 48×48 pix^2 (5290 instantaneous vectors), respectively. This is in close agreement to the corresponding smooth wall data. Even if the analysis is influenced by the parameter settings, it is believed that the relative difference between smooth and rough wall data do not change drastically. Therefore, this study supports the previous findings of the experimental evidence of the presence of UMZs in a hypersonic TBL along smooth walls (Williams et al. 2018; Cogo et al. 2022) and extends this finding to rough walls with only negligible differences between both wall conditions in case of the current transverse square bar topology ($\lambda/k = 4$). Due to the assumed connection to hairpin vortex structures, this would further support the notion that outer layer flow is not drastically affected by the investigated roughness.

4 Summary and outlook

In this paper PIV measurements along a 7° sharp cone at $Ma_\infty = 6$ and $Re_\infty = 16 \cdot 10^6$ 1/m with and without roughness were discussed. The rough wall consisted of two−dimensional transverse square bars with $\lambda/k \approx 4$, $k/\delta \approx 0.1$. The corresponding Reynolds numbers varied between $Re_\theta = 2770 - 6689$, $Re_{\delta 2} = 793 - 1288$ and $Re_\tau = 212{-}384$.

Van Driest transformed mean velocity profiles along the smooth wall agreed well in inner scaling with each other and with the incompressible law of the wall if the corresponding parameters, namely u_τ and Π, were fitted accordingly. The resulting parameters correspond well to previous investigations and are in a value range expected from fully turbulent profiles in the corresponding Reynolds number range. The rough wall fitting is a challenging procedure, mainly due to the considerable influence of the shift of origin, most likely due to the k/δ value range of the current data. A combination of an integral and fitting approach was used to quantify the friction velocity for the rough wall profiles. The combined approach resulted in inner scaled profiles with the expected shift ΔU_{eff}^+ due to roughness in the order of 6 with roughness Reynolds numbers in a range of $k^+ \approx 30 - 40$. Apart from that, rough wall profiles show in general larger wake parameters up to approximately 0.8, similar to previous studies.

The smooth wall turbulence profiles agreed to previous experimental data and artificially filtered DNS in case of the streamwise component, if the corresponding resolution of the PIV data is considered. Streamwise turbulence profiles above the smooth and rough wall agreed to within measurement accuracies.

Two−point velocity fluctuation correlation results showed that the general structure with respect to largest length−scales and structure angles are similar to within the scatter of the data in the outer layer above the smooth and rough wall. Only in close vicinity to the rough wall, length−scales decrease below the smooth wall data, comparable to results from other investigators. Data of this paper also support the notion from previous comparable investigations that correlation lengths are only moderately decreasing with Mach number.

Previous evidence for the existence of uniform momentum zones along smooth wall hypersonic turbulent boundary layers could be confirmed in this study and the evidence was extended to the investigated rough wall.

The observations that compressible smooth and rough wall turbulent profiles as well as corresponding largest length−scales and structure angles agree above a certain wall−normal distance, support the outer layer similarity argument, despite the rather large values of k/δ and low Reynolds numbers in this work. A potential explanation for the observation that Coles wake parameters do not agree but turbulence data do collapse in the outer layer was given by Castro et al. (2013) with potential transitional roughness effects, which cannot be excluded here completely. To clarify potential impacts of compressibility, roughness regimes and due to on−going debates about the applicability of the outer layer similarity (e.g., Castro et al. 2013; Flack et al. 2007; Antonia and Djenidi 2010; Schultz and Flack 2005), more data is necessary.

Acknowledgements The authors express their special acknowledgement to Michael Kosbow and Marco Schmors for their very efficient work with respect to the test preparation, facility and PIV preparation.

Author contribution Dominik Neeb's contribution to this work includes conceptualization, methodology, analysis, investigation, original draft preparation as well as editing. Pascal Marquardt was in charge of the PIV measurement implementation and execution, provided the PIV analysis code, contributed review, and technical expertise to this work. Ali Gülhan contributed review, funding acquisition, resources, and supervision to this work.

Funding Open Access funding enabled and organized by Projekt DEAL. This work was fully funded by the DLR's Program Directorate for Space Research and Development in the frame of space transportation research activities.

Code availability No datasets were generated or analyzed during the current study.

Declarations

Conflict of interest The authors have no relevant financial or non−financial interests to disclose.

Ethics approval Not applicable.

Consent to participate No special consent required for participation.

Consent for publication No special consent required for participation.

References

Adrian RJ, Meinhart CD, Tomkins CD (2000) Vortex organization in the outer region of the turbulent boundary layer. J Fluid Mech 422:1–54

Anderson JD (1990) Modern compressible flow: with historical perspective, vol 12. McGraw−Hill, New York

Antonia RA, Djenidi L (2010) On the outer layer controversy for a turbulent boundary layer over a rough wall. In IUTAM Symposium on The Physics of Wall−Bounded Turbulent Flows on Rough Walls: Proceedings of the IUTAM Symposium on The Physics of Wall−Bounded Turbulent Flows on Rough Walls, held Cambridge, UK, July 7–9, 2009 (pp. 77–86). Springer Netherlands

Arnette SA, Samimy M, Elliott GS (1995) Structure of supersonic turbulent boundary layer after expansion regions. AIAA J 33(3):430–438

Astarita T, Cardone G (2005) Analysis of interpolation schemes for image deformation methods in PIV. Exp Fluids 38:233–243

Bandyopadhyay PR (1987) Rough−wall turbulent boundary layers in the transition regime. J Fluid Mech 180:231–266

Benedict LH, Gould RD (1996) Towards better uncertainty estimates for turbulence statistics. Exp Fluids 22(2):129–136

Berg DE (1977) Surface roughness effects on the hypersonic turbulent boundary layer. Thesis, California Institute of Technology, Pasadena, California

Bettermann D (1966) Contribution a l'etude de la convection forcee turbulente le long de plaques rugueuses. Int J Heat Mass Transf 9(3):153–164

Bowersox RD, Latin RM (2001) Experimental Investigation Of High−Speed Boundary Layers with Wall Roughness. Final report UA−AEM−APL−2001–001

Castro IP (2007) Rough−wall boundary layers: mean flow universality. J Fluid Mech 585:469–485

Castro IP, Segalini A, Alfredsson PH (2013) Outer−layer turbulence intensities in smooth−and rough−wall boundary layers. J Fluid Mech 727:119–131

Choi YK, Hwang HG, Lee YM, Lee JH (2020) Effects of the roughness height in turbulent boundary layers over rod−and cuboid−roughened walls. Int J Heat Fluid Flow 85:108644

Choi YK (2021) Direct Numerical Simulations in Turbulent Boundary Layers over Rod−and Cuboid−roughened Walls: Effects of the Roughness Height, Master Thesis, Ulsan National Institute of Science and Technology.

Chung D, Hutchins N, Schultz MP, Flack KA (2021) Predicting the drag of rough surfaces. Annu Rev Fluid Mech 53:439–471

Cogo M, Salvadore F, Picano F, Bernardini M (2022) Direct numerical simulation of supersonic and hypersonic turbulent boundary layers at moderate−high Reynolds numbers and isothermal wall condition. J Fluid Mech 945:A30

de Silva CM, Philip J, Chauhan K, Meneveau C, Marusic I (2013) Multiscale geometry and scaling of the turbulent−nonturbulent interface in high Reynolds number boundary layers. Phys Rev Lett 111(4):044501

de Silva CM, Hutchins N, Marusic I (2016) Uniform momentum zones in turbulent boundary layers. J Fluid Mech 786:309–331

Duan L, Beekman I, Martin MP (2010) Direct numerical simulation of hypersonic turbulent boundary layers. Part 2. Effect of wall temperature. J Fluid Mech 655:419–445

Duan L, Beekman I, Martin MP (2011) Direct numerical simulation of hypersonic turbulent boundary layers. Part 3. Effect of Mach number. J Fluid Mech 672:245–267

Ekoto IW, Bowersox R, Beutner T, Goss L (2008) Supersonic boundary layers with periodic surface roughness. AIAA J 46(2):486–497

Fernholz, H. H., & Finley, P. J. (1980). *A critical commentary on mean flow data for two−dimensional compressible turbulent boundary layers* (p. 0230). North Atlantic Treaty Organization, Advisory Group for Aerospace Research and Development.

Flack KA, Schultz MP, Connelly JS (2007) Examination of a critical roughness height for outer layer similarity. Physics of Fluids, 19(9)

Ganapathisubramani B (2007) Statistical properties of streamwise velocity in a supersonic turbulent boundary layer. Phys Fluids 19(9):098108

Ganapathisubramani B, Clemens NT, Dolling DS (2006) Large−scale motions in a supersonic turbulent boundary layer. J Fluid Mech 556:271–282

Goddard, F. E. (1957) The effect of uniformly distributed roughness on turbulent skin friction drag at supersonic speeds," Thesis, California Institute of Technology, Pasadena, California,

Gülhan A, Willems S, Neeb D (2021) Shock interaction induced heat flux augmentation in hypersonic flows. Exp Fluids 62:1–18

Hannemann V (2002) S*tructured multigrid agglomeration on a data structure for unstructured meshes*. Int j Numer Methods Fluids 40(3–4):361–368

Hutchins N, Marusic I (2007) Evidence of very long meandering features in the logarithmic region of turbulent boundary layers. J Fluid Mech 579:1–28

Jiménez J (2004) Turbulent flows over rough walls. Annu Rev Fluid Mech 36:173–196

Klebanoff P (1955) Characteristics of turbulence in boundary layer with zero pressure gradient. Tech. Rep. NACA−TR−1247, National Bureau of Standards

Krogstad PÅ, Antonia RA, Browne LWB (1992) Comparison between rough−and smooth−wall turbulent boundary layers. J Fluid Mech 245:599–617

Krogstadt P−Å, Antonia RA (1999) Surface roughness effects in turbulent boundary layers. Exp Fluids 27(5):450–460

Latin RM, Bowersox RDW (2000) Flow properties of a supersonic turbulent boundary layer with wall roughness. AIAA J 38(10):1804–1821

Lee JH, Kevin M, J. P., & Hutchins, N. (2016) Validating under−resolved turbulence intensities for PIV experiments in canonical wall−bounded turbulence. Exp Fluids 57:1–11

Leonardi S, Orlandi P, Smalley RJ, Djenidi L, Antonia RA (2003) Direct numerical simulations of turbulent channel flow with transverse square bars on one wall. J Fluid Mech 491:229–238

Leonardi S, Orlandi P, Antonia RA (2007) Properties of d−and k−type roughness in a turbulent channel flow. Physics of fluids, 19(12)

Liu CK, Klein SJ, Johnston JP (1966) An experimental study of turbulent boundary layer on rough walls," No. MD−15. Stanford univ calif thermosciences div

Marquardt P, Klaas M, Schröder W (2020) Experimental investigation of the turbulent Schmidt number in supersonic film cooling with shock interaction. Exp Fluids 61(7):160

Marusic I, Heuer WD (2007) Reynolds number invariance of the structure inclination angle in wall turbulence. Phys Rev Lett 99(11):114504

Moore WL (1951). An experimental investigation of the boundary layer development along a rough surface (Doctoral dissertation, State University of Iowa)

Neeb D, Gülhan A, Merrifield JA (2016) Rough−wall heat flux augmentation analysis within the exomars project. J Spacecr Rocket 53(1):121–133

Neeb D, Saile D, Gülhan A (2018) Experiments on a smooth wall hypersonic boundary layer at Mach 6. Exp Fluids 59:1–21

Nikuradse, J., (1933).English Translation: Law of flow in rough pipes, *TM1292, NACA*, USA (in German: Stroemungsgesetze in rauhen Rohren. *Forsch. Ing. Wesen,* Heft 361)

Patel A, Peeters JW, Boersma BJ, Pecnik R (2015). Semi−local scaling and turbulence modulation in variable property turbulent channel flows. Physics of Fluids, 27(9)

Peltier SJ (2013) Behavior of turbulent structures within a Mach 5 mechanically distorted boundary layer (Doctoral dissertation).

Perry AE, Joubert PN (1963) Rough−wall boundary layers in adverse pressure gradients. J Fluid Mech 17(02):193–211

Perry AE, Li JD (1990) Experimental support for the attached−eddy hypothesis in zero−pressure−gradient turbulent boundary layers. J Fluid Mech 218:405–438

Perry AE, Schofield WH, Joubert PN (1969) Rough wall turbulent boundary layers. J Fluid Mech 37(2):383–413

Pirozzoli S, Bernardini M (2011) Turbulence in supersonic boundary layers at moderate Reynolds number. J Fluid Mech 688:120–168

Pritchett V, Bowersox R (2001) Flow properties of compressible and incompressible subsonic turbulent boundary layers with surface roughness. In 39th Aerospace Sciences Meeting and Exhibit (p. 1021)

Sahoo D, Marco S, Smits AJ "Effects of roughness on a turbulent boundary layer in hypersonic flow." AIAA Paper 3678 (2009).

Sahoo D, Michael P, Smits AJ "PIV experiments on a rough−wall hypersonic turbulent boundary layer." AIAA Paper 4471 (2010)

Scharnowski S, Bross M, Kähler CJ (2019) Accurate turbulence level estimations using PIV/PTV. Exp Fluids 60:1–12

Schlichting H (1936) Experimentelle Untersuchungen zum Rauhigkeitsproblem. Ingenieur−archiv 7(1):1–34. https://doi.org/10.1007/BF02084166

Schultz MP, Flack KA (2005) Outer layer similarity in fully rough turbulent boundary layers. Exp Fluids 38:328–340

Sillero JA, Jiménez J, Moser RD, (2013) One−point statistics for turbulent wall−bounded flows at Reynolds numbers up to δ+≈ 2000. Physics of Fluids, 25(10).

Sillero JA, Jiménez J, Moser RD, (2014) Two−point statistics for turbulent boundary layers and channels at Reynolds numbers up to δ+≈ 2000. Physics of Fluids, 26(10)

Smits AJ, Dussauge JP (2006) Turbulent shear layers in supersonic flow. Springer Science & Business Media

Townsend AAR (1976) The structure of turbulent shear flow. Cambridge University Press

Trettel A, Larsson J (2016) Mean velocity scaling for compressible wall turbulence with heat transfer. Physics of Fluids, 28(2).

Van Driest ER (2003) Turbulent boundary layer in compressible fluids. J Spacecr Rocket 40(6):1012–1028

Wang JX, Huang J, Duan L, Xiao H (2019) Prediction of Reynolds stresses in high−Mach−number turbulent boundary layers using physics−informed machine learning. Theoret Comput Fluid Dyn 33:1–19

Westerweel J, Scarano F (2005) Universal outlier detection for PIV data. Exp Fluids 39:1096–1100

White FM, Corfield I (2006) Viscous fluid flow, vol 3. McGraw−Hill, New York

Willems, Sebastian, et al. (2014) *Laminar to turbulent transition on the HIFiRE−1 cone at Mach 7 and high angle of attack. AIAA Paper* 428.

Williams OJ, Smits AJ (2017) Effect of tripping on hypersonic turbulent boundary−layer statistics. AIAA J 55(9):3051–3058

Williams OJ, Sahoo D, Baumgartner ML, Smits AJ (2018) Experiments on the structure and scaling of hypersonic turbulent boundary layers. J Fluid Mech 834:237–270

Williams OJ, Sahoo D, Papageorge M, Smits AJ (2021) Effects of roughness on a turbulent boundary layer in hypersonic flow. Exp Fluids 62:1–13

Williams OJ, Nguyen T, Schreyer AM, Smits AJ (2015) Particle response analysis for particle image velocimetry in supersonic flows. Physics of Fluids, 27(7)

Zhang C, Duan L, Choudhari MM (2018) Direct numerical simulation database for supersonic and hypersonic turbulent boundary layers. AIAA J 56(11):4297–4311